

Symmetry aware Reynolds Averaged Navier Stokes turbulence models with equivariant neural networks

Aaron Miller^{*1}, Sahil Kommalapati^{2, 3}, Robert Moser^{2, 3}, and Petros Koumoutsakos¹

¹Computational Science and Engineering Laboratory, Harvard University, MA 02138, USA

²Oden Institute for Computational Engineering and Sciences, The University of Texas at Austin, TX 78712, USA

³Department of Mechanical Engineering, The University of Texas at Austin, TX 78712, USA

November 14, 2025

Abstract

Accurate and generalizable Reynolds-averaged Navier-Stokes (RANS) models for turbulent flows rely on effective closures. We introduce tensor-based, symmetry aware closures using equivariant neural networks (ENNs) and present an algorithm for enforcing algebraic contraction relations among tensor components. The modeling approach builds on the structure tensor framework introduced by Kassinos and Reynolds to learn closures in the rapid distortion theory setting. Experiments show that ENNs can effectively learn relationships involving high-order tensors, meeting or exceeding the performance of existing models in tasks such as predicting the rapid pressure-strain correlation. Our results show that ENNs provide a physically consistent alternative to classical tensor basis models, enabling end-to-end learning of unclosed terms in RANS and fast exploration of model dependencies.

1 Introduction

Reynolds-averaged Navier-Stokes (RANS) models are a cornerstone of simulations for applications such as car and aircraft aerodynamics. Their lower cost, over higher-fidelity methods such as Direct Numerical Simulations (DNS) and Large Eddy Simulation (LES), makes RANS a practical and efficient choice, providing statistically averaged flow information rather than resolving every turbulent detail. In RANS, flow quantities are decomposed into mean and fluctuating contributions, and the governing Navier-Stokes equations are used to develop equations for the mean flow. These equations involve terms such as the Reynolds stresses that need to be evaluated, leading to the closure problem in RANS modeling¹.

A popular approach for closing RANS equations is to adopt the linear turbulent-viscosity hypothesis, which proposes that the Reynolds stresses are proportional to the mean velocity gradients, analogous to the viscous stress relation for a Newtonian fluid. Although computationally efficient

^{*}Correspondence to aaronmiller@g.harvard.edu

¹Throughout this work, the term *closure*, indicates a model of a particular flow variable appearing in the governing equations, in contrast to use of the term to indicate a correction added to remedy modeling or discretization error.

and simple to implement, the linear turbulent-viscosity assumption does not hold for many important flow conditions, particularly those that include curved geometries or separation [1]. Nonlinear turbulent-viscosity models, which feature higher-order products of the mean strain rate and rotation rate tensors, have also been proposed [2]. An alternative closure approach that avoids the turbulent-viscosity assumption involves solving transport equations for the Reynolds stresses directly. As Reynolds stresses are the second moments of velocity, these are referred to as second-order closure models [3].

All of these closure strategies involve constitutive relations, which are modeled by tensor valued functions of tensor inputs. The structure of these functions is constrained by the known transformation properties of the tensors under symmetry groups. Hence, it is essential that a model preserves the tensor structure of its inputs and outputs so that the implied physics remains coordinate system invariant. This notion is fundamental in turbulence modeling [1, 4], and is further emphasized with the rise of data driven approaches [5, 6].

This paper is based on the premise that function invariance and equivariance are critical to the design of turbulence models. We construct symmetry-consistent RANS closure models by representing tensor functions as equivariant neural networks (ENNs). Although previous approaches require a priori tensor analysis to ensure physical validity, ENNs can enforce several classes of symmetry properties as hard constraints through architecture design. This paper presents an algorithm that broadens the types of constraint that ENNs can enforce and their application to RANS modeling. The primary contributions of the paper are:

- Introduction of a novel algorithm and corresponding ENN layer that exactly enforces linear tensor relationships, extending the symmetry-preserving properties of ENNs to a new class of constraints beyond equivariance and index permutation symmetries. We note that, although applied here to RANS, the method is general and can be used in other domains without modification.
- Experiments on new rapid distortion theory data demonstrating that ENNs achieve state-of-the-art results on a sequence of RANS modeling tasks, yielding order-of-magnitude lower errors in certain distortion regimes.
- First presentation of models featuring general nonlinear stropholysis tensor dependence in the RANS modeling framework pioneered by Kassinos and Reynolds [7], in addition to a broader group-theoretic analysis of the turbulent structure tensors.

In Sect. 2, we review previous approaches for the representation of equivariant tensor functions in RANS modeling, as well as the development of ENNs in the broader machine learning literature. Sect. 3 describes the problem setting and Sect. 4 the representation theory of tensors, how it informs the design of the ENN structure and the proposed algorithm to enforce the linear tensor constraints. Sec. 5 describes data generation and results. Finally, Sec. 6 concludes with a discussion and outlook.

2 Related Work

2.1 Invariant theory for tensor function representation

The dominant approach in fluid mechanics to build equivariant tensor functions was initiated in [8] and applies the theory of invariants to represent tensor functions as a linear combination of basis tensors [3, 9–14]. The expansion coefficients are, in general, functions of tensor invariants.

Although the form of these coefficients must be determined by other means, this approach satisfies the appropriate symmetry properties while reducing the modeling problem to the determination of scalar functions of scalar arguments. This approach is here referred to as the *tensor basis method* (TBM).

Analytical methods for determining the coefficient functions include treating them as constants, forming expressions from Taylor expansions [10], or deriving other non-polynomial forms [3]. The drawback to such approaches is that they rely on a priori assumptions or require truncation. Alternatively, the tensor basis neural network (TBNN), introduced by [11] and applied in [15–17], among others, uses neural networks to parameterize the coefficient functions. The universal approximation property of neural networks implies that this construction remains theoretically general, and since the coefficient functions are scalar functions of scalars, any network architecture can be used without violating symmetry constraints.

The TBM has been used successfully for several turbulence modeling problems, for example predicting the Reynolds stress anisotropy and improving mean velocity predictions in square duct, wavy wall, curved backward-facing step, and right-angled backward facing step geometries [11, 12], as well as for modeling tasks in other areas of fluid mechanics, for example learning rheological constitutive equations [16, 18]. However, it is limited by the need to derive the tensor basis, which determines both the number of coefficient functions and their arguments. Deriving a minimal basis and the associated invariants is a challenging task. The size of the minimal integrity bases grows exponentially with the number of tensor arguments, and the results are only available for a limited number of special cases [14, 19–21]. Moreover, a newly derived basis is necessary when the model dependencies change. This motivates the search for alternative modeling procedures that satisfy the relevant symmetry constraints and maintain generality but do not require a priori derivation of basis tensors and their invariants.

2.2 Equivariant neural networks

The architectures of equivariant neural networks are distinguished by the way in which they handle geometric attributes [22]. Some approaches use only scalar features, such as norms or triplet angles, as input to the network instead of higher-order tensors [23, 24]. While this guarantees invariance to Euclidean transformations, it comes at the cost of expressivity. Moreover, pre-computation of the derived scalars becomes increasingly complex with an increasing number and tensor order of the inputs. Alternatively, equivariant architectures aim to retain full geometric information by operating on tensors directly. The developments that most inform the present work include those in [25–28], which make use of the notion of irreducible representations. Working directly with the fundamental building blocks of group representations provides a framework for generalizing equivariant operations to higher-order tensors, a task that is particularly relevant to RANS applications. ENNs have been used in particular to obtain state of the art property predictions in molecular dynamics simulations [29–32]. These results have demonstrated the efficacy of operating directly on geometric attributes. The TBM, discussed above, applies machine learning only to the *invariant* parts of the problem, relying on analytical treatment of the *equivariant* aspects offline.

An equivariant closure modeling strategy that avoids offline basis derivation is the vector cloud neural network (VCNN-e) [33, 34], which maps a cloud of local flow or geometry features to the Reynolds stresses via an invariant embedding and an equivariant output map. However, it only considers vectorial features and does not provide a framework for enforcing general index-permutation symmetries or prescribed linear constraints. Another approach targeting equivariant tensorial constitutive relations is RotEqNet [35], which uses position standardization to map rotated inputs to a canonical orientation. For higher order tensors, contractions are used to compute a rotation into the

standard position. A model is trained on the standardized inputs and the predictions are rotated back to the original frame for inference. This method is restricted to fully symmetric tensors and guarantees exact equivariance only when the model in the standardized frame is learned perfectly. The work of [36] explores the use of irreducible representation-based equivariant networks in the RANS context but differs from the present study in several key respects. First, the model in [36] is trained to learn single-injection corrections based on the converged output of a particular RANS model. This limits the applicability of the model to input associated with the RANS solver used to generate training data. In contrast, this work learns constitutive relations between terms in the governing equations, and hence completes a RANS model rather than corrects it. Furthermore, the present work targets Reynolds stress models and does not restrict the focus to steady problems.

Equivariant networks have also been applied to problems in fluid dynamics beyond turbulence modeling. One line of research extends the mesh-based graph neural network (GNN) surrogate framework introduced in [37]. For example, [38] applies the Steerable Equivariant Graph Neural Network architecture to Lagrangian fluid mechanics, providing a direct comparison to non-equivariant surrogates. Related GNN approaches employ an encode-process-decode strategy, but modify the treatment of vector features to enforce equivariance, either by transforming them into local strain eigenbases [39] or by projecting them onto graph edges [40].

2.3 Integrating Physics Constraints in Machine Learning models

Integrating physical priors into machine learning models aims to improve their data efficiency and predictive accuracy. To our knowledge, the first work in this field integrated wall shear stresses and pressure gradients to improve the neural network forecast of near wall flow in turbulent channel flows [41]. Physics informed machine learning models such as PINNs [42–44] embed physics constraints by regularizing the loss function with a term that penalizes deviations from known PDE governing equations. In order to achieve equivariance, a straightforward approach is data augmentation, in which symmetry operations are applied to the training data [45]. However, at least for continuous symmetry groups, it is impossible to generate data for every possible symmetry transformation, and there is no guaranty that the model will satisfy equivariance.

Alternatively, *hard constraints* reduce the search space for optimization and ensure physical consistency by construction. Examples of this approach include [46–48]. The tools described here also fall into the hard constraint category. ENNs are equivariant by construction and can be designed to respect index permutation symmetries, such as the symmetric tensor. In this paper, a method is developed for enforcing another class of tensor relationships, namely “einsum”-style linear relations, as hard constraints in ENNs. Einsum is a generalized Einstein summation notation to represent arbitrary linear maps and relations, that can extend beyond standard tensor contractions and has found extensive applications in machine learning. An einsum-like domain-specific language is the basis for the Tensor Comprehensions [49] library in PyTorch, which automatically generates GPU code and auto-tunes it for specific input sizes.

3 The Reynolds-Averaged Navier-Stokes (RANS)

We outline Reynolds stress modeling for incompressible Newtonian fluids. We refer the reader to [1] for a thorough handling of the subject.

The RANS framework is based on a decomposition of flow variables into a mean component and a random fluctuation. Let \mathbf{U} denote the instantaneous fluid velocity field and \mathbf{u} denote the

fluctuating velocity field in Reynolds decomposition

$$\mathbf{U} = \langle \mathbf{U} \rangle + \mathbf{u},$$

where the averaging operator $\langle \cdot \rangle$ is defined as the expectation

$$\langle \mathbf{U}(\mathbf{x}, t) \rangle \equiv \iiint_{-\infty}^{\infty} \mathbf{V} f(\mathbf{V}; \mathbf{x}, t) dV_1 dV_2 dV_3,$$

with $f(\mathbf{V}; \mathbf{x}, t)$ the probability density function of the velocity field at position \mathbf{x} and time t ². The evolution of the mean velocity is governed by the Reynolds equations³:

$$\nabla \cdot \langle \mathbf{U} \rangle = 0, \quad (1)$$

$$\frac{\bar{D}\langle U_j \rangle}{\bar{D}t} = -\frac{1}{\rho} \frac{\partial \langle p \rangle}{\partial x_j} + \nu \nabla^2 \langle U_j \rangle - \frac{\partial \langle u_i u_j \rangle}{\partial x_i}, \quad (2)$$

where $p = \langle p \rangle + p'$ is the pressure, ν is the (constant) kinematic viscosity, and

$$\frac{\bar{D}}{\bar{D}t} \equiv \frac{\partial}{\partial t} + \langle U_j \rangle \frac{\partial}{\partial x_j}$$

is the (mean) material derivative. The closure problem in RANS refers to the fact that in 2 we need to specify the evolution of the Reynolds stresses $\langle u_i u_j \rangle$. This paper focuses on Reynolds stress models that solve transport equations for Reynolds stresses.

3.1 Reynolds stress modeling

The exact transport equations for the Reynolds stresses can be derived from Eqs. 1 and 2:

$$\frac{\bar{D}\langle u_i u_j \rangle}{\bar{D}t} + \frac{\partial \langle u_i u_j u_k \rangle}{\partial x_k} = \nu \nabla^2 \langle u_i u_j \rangle + \mathcal{P}_{ij} + \Pi_{ij} - \varepsilon_{ij},$$

where

$$\begin{aligned} \mathcal{P}_{ij} &\equiv -\langle u_i u_k \rangle \frac{\partial \langle U_j \rangle}{\partial x_k} - \langle u_j u_k \rangle \frac{\partial \langle U_i \rangle}{\partial x_k}, \quad \Pi_{ij} \equiv -\frac{1}{\rho} \left\langle u_i \frac{\partial p'}{\partial x_j} + u_j \frac{\partial p'}{\partial x_i} \right\rangle, \\ \text{and} \quad \varepsilon_{ij} &\equiv 2\nu \left\langle \frac{\partial u_i}{\partial x_k} \frac{\partial u_j}{\partial x_k} \right\rangle \end{aligned}$$

are the production tensor, the velocity-pressure gradient tensor, and the dissipation tensor, respectively. In turn, the production tensor can be decomposed as

$$\Pi_{ij} = \mathcal{R}_{ij} - \frac{\partial T_{kij}^{(p)}}{\partial x_k},$$

where

$$\mathcal{R}_{ij} \equiv \left\langle \frac{p'}{\rho} \left(\frac{\partial u_i}{\partial x_j} + \frac{\partial u_j}{\partial x_i} \right) \right\rangle \quad \text{and} \quad T_{kij}^{(p)} \equiv \frac{1}{\rho} \langle u_i p' \rangle \delta_{jk} + \frac{1}{\rho} \langle u_j p' \rangle \delta_{ik}$$

²The semicolon notation denotes the fact that f is a density with respect to \mathbf{V} at a particular position and time, and an alternative notation would be $f_{(\mathbf{x}, t)}(\mathbf{V})$.

³Throughout this work, we use the Einstein summation convention in which repeated indices apply summation, unless the indices are Greek letters.

are the pressure-rate-of-strain tensor and the pressure transport, respectively. Defining the Reynolds stress flux $T_{kij} \equiv T_{kij}^{(p)} + T_{kij}^{(u)} + T_{kij}^{(\nu)}$, where $T_{kij}^{(u)} \equiv \langle u_i u_j u_k \rangle$ and

$$T_{kij}^{(\nu)} \equiv -\nu \frac{\partial \langle u_i u_j \rangle}{\partial x_k},$$

we get the Reynolds stress transport equation

$$\frac{\bar{D}\langle u_i u_j \rangle}{\bar{D}t} + \frac{\partial T_{kij}}{\partial x_k} = \mathcal{P}_{ij} + \mathcal{R}_{ij} - \varepsilon_{ij},$$

We note that this equation is exact. The pressure-rate-of-strain tensor can be broken up into three contributions corresponding to the terms in a decomposition of fluctuating pressure p' . The Poisson equation for p' is

$$\frac{1}{\rho} \nabla^2 p' = -2 \frac{\partial \langle U_i \rangle}{\partial x_j} \frac{\partial u_j}{\partial x_i} - \frac{\partial}{\partial x_i \partial x_j} (u_i u_j - \langle u_i u_j \rangle),$$

which motivates the definitions of $p^{(r)}$, $p^{(s)}$, and $p^{(h)}$ as the quantities that satisfy

$$\frac{1}{\rho} \nabla^2 p^{(r)} = -2 \frac{\partial \langle U_i \rangle}{\partial x_j} \frac{\partial u_j}{\partial x_i}, \quad \frac{1}{\rho} \nabla^2 p^{(s)} = -\frac{\partial^2}{\partial x_i \partial x_j} (u_i u_j - \langle u_i u_j \rangle), \quad \text{and} \quad \nabla^2 p^{(h)} = 0,$$

respectively. The corresponding pressure-rate-of-strain tensors are then

$$\mathcal{R}_{ij}^{(\cdot)} \equiv \left\langle \frac{p^{(\cdot)}}{\rho} \left(\frac{\partial u_i}{\partial x_j} + \frac{\partial u_j}{\partial x_i} \right) \right\rangle, \quad (3)$$

where the dot in (\cdot) is one of $\{r, s, h\}$. The Reynolds stress transport may then be written as

$$\frac{\bar{D}\langle u_i u_j \rangle}{\bar{D}t} + \frac{\partial T_{kij}}{\partial x_k} = \mathcal{P}_{ij} + \mathcal{R}_{ij}^{(r)} + \mathcal{R}_{ij}^{(s)} + \mathcal{R}_{ij}^{(h)} - \varepsilon_{ij}. \quad (4)$$

The last term on the left-hand side and the last four terms on the right-hand side require closures. Among them, those corresponding to the pressure-rate-of-strain are the most important quantities to model. For certain classes of flows, many of the terms in Eq. 4 drop out. This allows us to focus on particular parts of the closure problem. Examples include the return-to-isotropy problem and the limit of rapid distortion theory (RDT), which isolate the tasks of modeling $\mathcal{R}_{ij}^{(s)}$ and $\mathcal{R}_{ij}^{(r)}$, respectively.

Additional quantities of turbulence that will appear in the following include the turbulent kinetic energy and dissipation, which are given by

$$k \equiv \frac{1}{2} \langle u_i u_i \rangle \quad \text{and} \quad \varepsilon \equiv 2\nu \langle s_{ij} s_{ij} \rangle = \frac{1}{2} \varepsilon_{ii},$$

respectively, where s_{ij} is defined through the decomposition of the strain rate tensor as

$$S_{ij} \equiv \frac{1}{2} \left(\frac{\partial U_i}{\partial x_j} + \frac{\partial U_j}{\partial x_i} \right) = \langle S_{ij} \rangle + s_{ij}.$$

For normalization purposes, sometimes $q^2 \equiv \langle u_i u_i \rangle = 2k$ is used instead of k .

3.2 Rapid distortion theory

The RDT limit describes flows for which the turbulence-to-mean-shear time scale ratio $\mathcal{S}\tau = \mathcal{S}k/\varepsilon$, where $\mathcal{S} \equiv (2\langle S_{ij} \rangle \langle S_{ij} \rangle)^{1/2}$, is arbitrarily large [1]. In RDT the governing equations for \mathbf{u} and $p^{(r)}$ can be obtained from the transport equation for fluctuating velocity and the Poisson equation for p' by keeping only the dominant terms, which are those that scale with \mathcal{S} .

The Reynolds stress transport equation (Eq. 4) in the RDT limit is expressed as

$$\frac{d\langle u_i u_j \rangle}{dt} = \mathcal{P}_{ij} + \mathcal{R}_{ij}^{(r)} = -\langle u_j u_k \rangle \frac{\partial \langle U_i \rangle}{\partial x_k} + \langle u_i u_k \rangle \frac{\partial \langle U_j \rangle}{\partial x_k} + 2 \frac{\partial \langle U_l \rangle}{\partial x_k} (M_{kjil} + M_{ikjl}),$$

where

$$M_{ijkl} \equiv \iiint_{-\infty}^{\infty} \Phi_{ij} \frac{\kappa_k \kappa_l}{\kappa^2} d\kappa \quad (5)$$

is a fourth-order tensor defined in terms of the velocity spectrum tensor

$$\Phi_{ij}(\kappa) \equiv \frac{1}{(2\pi)^3} \iiint_{-\infty}^{\infty} R_{ij}(\mathbf{r}) e^{-i\kappa \cdot \mathbf{r}} d\mathbf{r},$$

which is the Fourier transform of the two-point correlation $R_{ij}(\mathbf{r}, t) \equiv \langle u_i(\mathbf{x}, t) u_j(\mathbf{x} + \mathbf{r}, t) \rangle$.

The closure problem in RDT is to find a model for the rapid pressure tensor $\mathcal{R}_{ij}^{(r)}$, or equivalently for \mathbf{M} . In [7], it is argued that Reynolds stresses alone do not express a sufficiently rich description of the statistical characteristics of turbulence. Instead, the authors propose that a set of structure tensors, which describe both the dimensionality and componentality of the turbulent statistics, can form the basis of a reliable model. The governing equations involving the structure tensors are (see [50])

$$\frac{d\langle u_i u_j \rangle}{dt} = -\frac{\partial \langle U_i \rangle}{\partial x_m} \langle u_m u_j \rangle - \frac{\partial \langle U_j \rangle}{\partial x_m} \langle u_m u_i \rangle + 2 \frac{\partial \langle U_n \rangle}{\partial x_m} (M_{inmj} + M_{jmni}), \quad (6)$$

$$\frac{dD_{ij}}{dt} = -D_{ik} \frac{\partial \langle U_k \rangle}{\partial x_j} - D_{jk} \frac{\partial \langle U_k \rangle}{\partial x_i} + 2\langle S_{mn} \rangle L_{imnj} - 2\langle S_{mn} \rangle M_{mni}, \quad (7)$$

$$\begin{aligned} \frac{dQ_{ijk}}{dt} = & -\langle \Omega_{mk} \rangle Q_{ijm} - \langle \Omega_{jm} \rangle Q_{imk} + 2\varepsilon_{its} \langle \Omega_{wq} \rangle M_{sqwjtk} \\ & - \varepsilon_{its} \langle \Omega_{sm} \rangle M_{jmtk} - \varepsilon_{its} \langle \Omega_{mt} \rangle M_{jsmk} \\ & - \frac{2}{3} \langle S_{pp} \rangle Q_{ijk} - \langle S_{mk}^* \rangle Q_{ijm} - 3\langle S_{jm}^* \rangle Q_{imk} - 3\langle S_{sl}^* \rangle \varepsilon_{its} M_{jlk} - \langle S_{sl}^* \rangle \varepsilon_{ist} M_{jtk} \\ & + 2\varepsilon_{itw} \langle S_{wj}^* \rangle D_{tk} - 2\varepsilon_{ijt} \langle S_{qw}^* \rangle (L_{qwkt} + M_{qwkt}) - 2\varepsilon_{itw} \langle S_{wq}^* \rangle L_{qjkt} \\ & + 4\langle S_{wq}^* \rangle J_{ijkwq}, \end{aligned} \quad (8)$$

where the new tensors appearing are provided in App. 8.1 to avoid clutter⁴. Eqs. 6-8 introduce additional closure problems, namely for the fourth-order tensor \mathbf{L} and the fifth-order tensor \mathbf{J} .

In summary, closure models are required for: \mathbf{M} , \mathbf{L} , and \mathbf{J} as functions of $\langle u_i u_j \rangle$, \mathbf{D} , and \mathbf{Q}^* , where $\mathbf{Q}^* = \text{Sym}(\mathbf{Q})$ is the fully symmetric part of \mathbf{Q} .

The reason for considering \mathbf{Q}^* is to avoid redundancy. As $\langle u_i u_j \rangle$ and \mathbf{D} are related to \mathbf{Q} via $\langle u_i u_j \rangle = \varepsilon_{jsr} Q_{sir}$ and $D_{ij} = \varepsilon_{irs} Q_{srj}$, \mathbf{Q}^* represents the information in \mathbf{Q} not contained in $\langle u_i u_j \rangle$ and \mathbf{D} [50]. In addition to cleanly separating dependencies, this requires fewer components to be passed as input to an ENN. After models for \mathbf{M} , \mathbf{L} , and \mathbf{J} are found, Eqs. 6-8 constitute a closed system for $\langle u_i u_j \rangle$, \mathbf{D} , and \mathbf{Q} .

⁴Only the tensor orders and their index symmetries are relevant from a methodological perspective, which is the focus of this work.

4 Methodology

The theoretical foundations of ENNs draw extensively on group and representation theory, as these closely related fields provide a natural way to formalize symmetry relationships. In this paper, relevant definitions and results are recalled as needed and further details are included found in App. 8.3. For a more complete description the reader is referred to [51, 52].

4.1 Cartesian tensors and spherical tensors

Flow variables in an RANS models are attributed geometric characteristics in a three-dimensional Euclidean space and are represented as Cartesian tensors.

Definition 4.1 (Cartesian tensor). A generalized Cartesian tensor of order n and signature $s \in \{0, 1\}$ is a quantity defined by its $3n$ components in a Cartesian coordinate system, which transform according to the following rule under an orthogonal coordinate transformation described by the matrix $\mathbf{R} \in \mathbb{R}^{3 \times 3}$:

$$T'_{i_1 i_2 \dots i_n} = (\det(\mathbf{R}))^s \sum_{i_1=1}^3 \sum_{i_2=1}^3 \dots \sum_{i_n=1}^3 R_{i_1 j_1} R_{i_2 j_2} \dots R_{i_n j_n} T_{j_1 j_2 \dots j_n}. \quad (9)$$

A vector is a Cartesian tensor of rank one.

The signature s determines a tensor's parity or its behavior under reflection. It extends the strict definition of a Cartesian tensor to describe quantities that behave differently under improper rotations, but are still often relevant to consider. For example, under improper rotation \mathbf{R} , quantities such as velocity, force, and electric field transform as $T'_i = R_{ij} T_j$, while quantities such as angular momentum, torque, and magnetic field transform as $T'_i = -R_{ij} T_j$. Vectors and tensors with $s = 1$ are called pseudovectors and pseudotensors, respectively.

Many useful tools become available by viewing Def. 4.1 from a group theoretic perspective. The orthogonal transformations $\{\mathbf{R} \in \mathbb{R}^{3 \times 3} | \mathbf{R}^T \mathbf{R} = 1\}$ form a group, namely the orthogonal group $O(3)$, under matrix multiplication, and the collection of tensors of a given order and dimensionality constitute a vector space. Hence, Eq. 9 essentially defines a Cartesian tensor as a collection of components that transform according to a particular representation of $O(3)$, namely the tensor product representation.

Although this representation is an intuitive generalization of the familiar matrix-vector product for rotating a vector, it is reducible, meaning that it contains at least one nontrivial invariant subspace. It is desirable to work with irreducible representations, as this makes it clear which operations are allowable when interacting tensors, for example in a neural network. If a representation is compact, it can be decomposed as a direct sum of irreducible representations via a change-of-basis. The bases that achieve this for $O(3)$ motivate the definition of spherical tensors⁵.

Definition 4.2 (Spherical tensor). A spherical tensor of order ℓ and parity $p \in \{-1, 1\}$ is a set of $2\ell+1$ components, denoted $T_m^{(\ell,p)}$, where m takes on integer values $-\ell, -\ell+1, \dots, \ell$ ⁶, that transform

⁵The more common setting in which spherical tensors appear is quantum mechanics, where there is the notion of a spherical tensor *operator*, and the definition presented here is formulated to mirror Def. 4.1, and although it is not the same as the quantum mechanical one, it represents the same core idea of components mixing within a single irreducible subspace of the rotation group.

⁶The symmetric indexing used here, while different from the standard zero-based indexing $0, 1, \dots$, is standard in the equivariant machine learning literature and has its roots in quantum mechanics.

under a coordinate transformation $\mathbf{R} \in \mathrm{O}(3)$ as

$$T_m'^{(\ell,p)} = p^{(1-\det(\mathbf{R}))/2} \sum_{m'=-\ell}^{\ell} \mathcal{D}_{mm'}^{(\ell)}(\hat{\mathbf{R}}) T_{m'}^{(\ell,p)}, \quad (10)$$

where $\hat{\mathbf{R}} = \det(\mathbf{R})\mathbf{R}$ is the pure rotational part of \mathbf{R} and $\mathcal{D}_{mm'}^{(\ell)}(\hat{\mathbf{R}})$ are the matrix elements of the order- ℓ irreducible representation of the special orthogonal group $\mathrm{SO}(3)$. The $(2\ell+1) \times (2\ell+1)$ matrices $\mathbf{D}^{(\ell)}(\hat{\mathbf{R}})$ are known as the Wigner-D matrices. It is convenient to define⁷

$$\hat{\mathbf{D}}^{(\ell)}(\mathbf{R}) = p^{(1-\det(\mathbf{R}))/2} \mathbf{D}^{(\ell)}(\hat{\mathbf{R}}),$$

such that the above definition may also be written as

$$T_m'^{(\ell,p)} = \sum_{m'=-\ell}^{\ell} \hat{\mathcal{D}}_{mm'}^{(\ell)}(\mathbf{R}) T_{m'}^{(\ell,p)}.$$

We introduce an example to illustrate the above ideas. Let \mathbf{T} be a second-order tensor in three dimensions. The nine components of \mathbf{T} belong to a nine-dimensional vector space V . In the Cartesian basis, these components transform as under a rotation in $\mathrm{O}(3)$ as

$$T'_{ij} = \sum_{k,l} R_{ik} R_{jl} T_{kl}.$$

To see how this action corresponds to a tensor product representation, note that the right-hand side may be written as $(\mathbf{R} \otimes_{\mathrm{kr}} \mathbf{R}) \mathrm{vec}(\mathbf{T})$, where \otimes_{kr} denotes the Kronecker product of two matrices, and $\mathrm{vec}(\mathbf{T})$ denotes the C-style flattening of \mathbf{T} . This matrix-vector product is illustrated in Fig. 1. The tensor product representation of two irreducible representations is generally not irreducible, as can be seen in the figure by the fact that $\mathbf{R} \otimes_{\mathrm{kr}} \mathbf{R}$ is a dense matrix.

As $\mathrm{O}(3)$ is a compact group, it can be decomposed as a direct sum of irreducible representations. That is, a change-of base exists such that all elements of the representation assume a block-diagonal form, with each block (an instance of $\hat{\mathbf{D}}^{(\ell)}(\mathbf{R})$) operating on an irreducible subspace (a spherical tensor) independently. These irreducible subspaces are sometimes called *steerable* vector spaces to reflect the additional structure supplied by the representation [26, 54]. In practice, a change-of base matrix can be built from solutions $\mathbf{S}^{(\ell)}$ that satisfy

$$\hat{\mathbf{D}}^{(\ell)}(\mathbf{R}) \mathbf{S}^{(\ell)} = \mathbf{S}^{(\ell)} \rho(\mathbf{R}), \quad \forall \mathbf{R} \in \mathrm{O}(3), \quad (11)$$

where $\hat{\mathbf{D}}^{(\ell)}(\mathbf{R})$ is an irreducible representation of order- ℓ and $\rho(\mathbf{R})$ is an arbitrary representation, for example $\mathbf{R} \otimes_{\mathrm{kr}} \mathbf{R}$ (The superscript on $\mathbf{S}^{(\ell)}$ is added to keep track of the irreducible representation the solution intertwines). According to Schur's lemma, a solution to Eq. 11 exists if and only if the irreducible representation of order- ℓ is contained in ρ . Furthermore, the dimension of the solution space is equal to the number of copies of the irreducible representation of order- ℓ in the decomposition, known as the multiplicity of the irreducible representation.

A change-of base matrix \mathbf{S}_ρ for the entire space of tensor components is obtained by solving Eq. 11 for increasingly higher ℓ , stopping when the sum of dimensions of all solutions, including

⁷A more explicit notation would include the parity, for example $\hat{\mathbf{D}}^{(\ell,p)}(\mathbf{R})$, but this is avoided for clarity. The hat notion is used instead to simultaneously reflect the connection to the Wigner-D matrices and mark the distinction that comes from considering $\mathrm{O}(3)$ instead of $\mathrm{SO}(3)$.

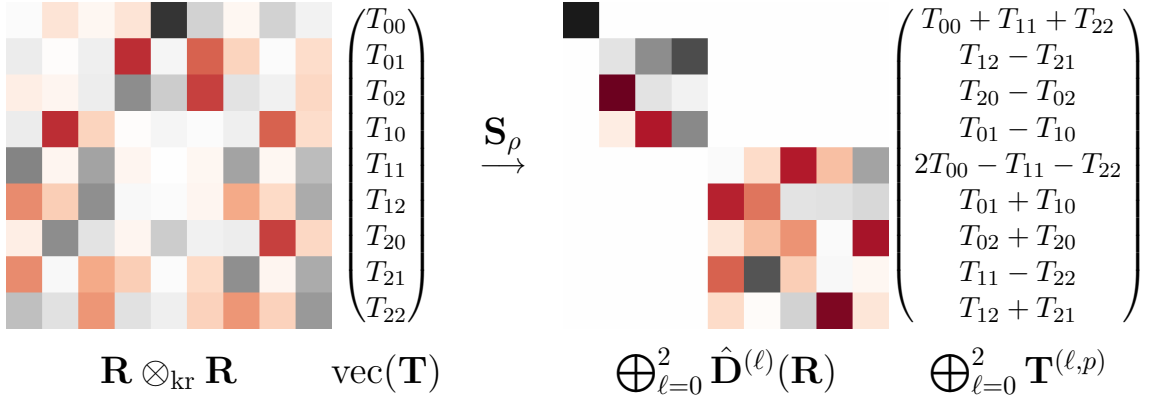


Figure 1: Decomposing a vector space into irreducible representation subspaces. The colored matrices represent an arbitrary element of an $O(3)$ representation; the vectors show the components in the basis of the matrix representation. Left: An element of $O(3)$ acts via the tensor product representation $\mathbf{R} \otimes_{kr} \mathbf{R}$, which is reducible. Right: A change-of-basis matrix \mathbf{S}_ρ exists that decomposes the tensor product representation into a direct sum of irreducible representations. Some of these irreducible subspaces may be ignored given index permutation symmetries, and particular component values may be fixed by linear tensor constraints. Visualization inspired by [53].

multiplicities, is equal to the dimension of ρ . Concretely, \mathbf{S}_ρ is the square matrix formed by stacking individual solutions vertically:

$$\mathbf{S}_\rho = \begin{pmatrix} \mathbf{S}^{(\ell_1)} \\ \mathbf{S}^{(\ell_2)} \\ \vdots \\ \mathbf{S}^{(\ell_n)} \end{pmatrix}. \quad (12)$$

The rows of \mathbf{S}_ρ that correspond to a given subspace are a basis for that subspace. Choosing the rows to be orthonormal, one can convert the tensor components in $\text{vec}(\mathbf{T})$, originally on the Cartesian basis, into the irreducible or spherical basis with the operation $\mathbf{S}_\rho \text{vec}(\mathbf{T})$. The flattened tensors expressed in the spherical basis are thus a direct sum of the spherical tensors. The different bases (Cartesian vs. spherical) and the associated structure of the representations are illustrated in Fig. 1.

4.2 Equivariance

A tensorially correct RANS model should not depend on the coordinate system used to express the flow variables [5]. For example, a second-order tensor-valued function \mathbf{f} of a second-order tensor \mathbf{x} should satisfy $\mathbf{R}\mathbf{f}(\mathbf{x})\mathbf{R}^T = \mathbf{f}(\mathbf{R}\mathbf{x}\mathbf{R}^T)$ for an arbitrary rotation \mathbf{R} . Intuitively, this says that the change in the component values from evaluating \mathbf{f} on a transformed input should be entirely due to the change in *perspective* stemming from the rotation of the coordinate system, such that the underlying physics implied by the function remains unchanged. For this reason, such functions are often referred to as isotropic tensor functions⁸. This notion is precisely captured by the definition of a function as being equivariant to the action of a symmetry group.

⁸Isotropic tensor *functions* are not to be confused with isotropic *tensors*, which are tensors whose components are the same in all rotated coordinate systems, and the use of the term “isotropic” across these contexts has historically caused some confusion [4].

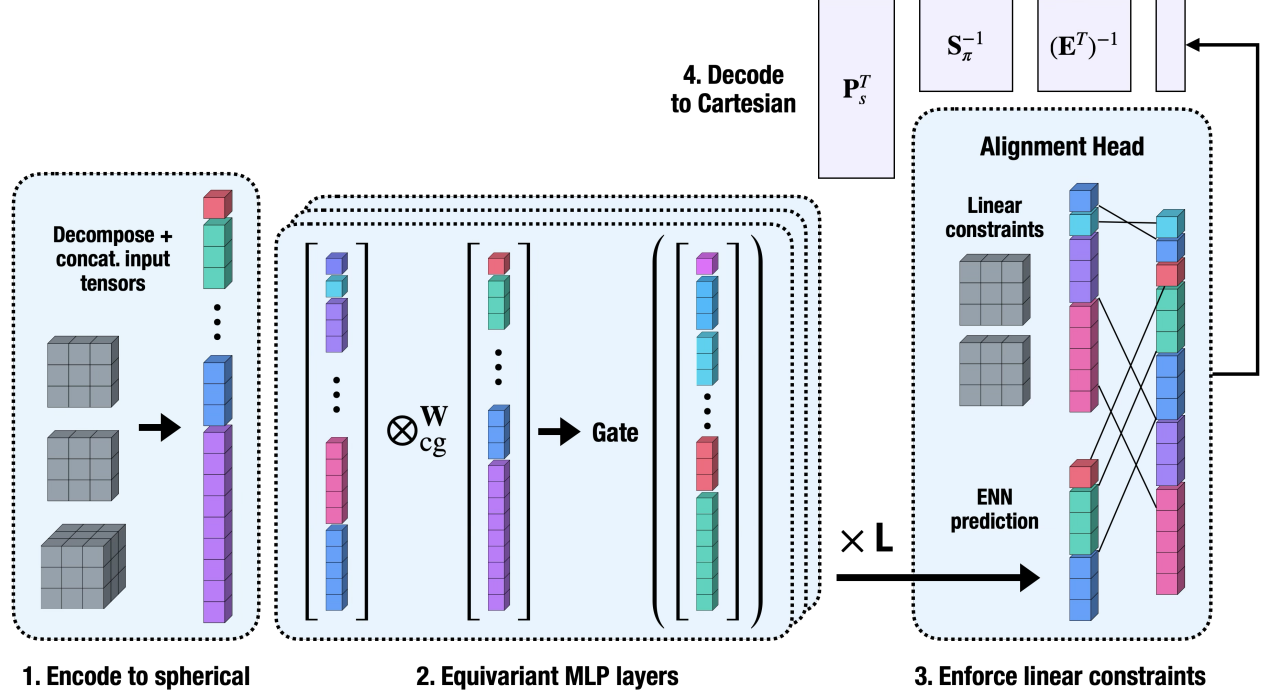


Figure 2: ENN architecture.

Definition 4.3 (Equivariance). Let X and Y be vector spaces. The function $\phi : X \rightarrow Y$ is equivariant with respect to a group G if it satisfies

$$\rho^Y(g)[\phi(x)] = \phi(\rho^X(g)[x]), \quad \text{or diagrammatically} \quad \begin{array}{ccc} X & \xrightarrow{\phi} & Y \\ \rho^X(g) \downarrow & & \downarrow \rho^Y(g) \\ X & \xrightarrow{\phi} & Y \end{array}$$

for all $g \in G$ and all $x \in X$, where $\rho^X : G \rightarrow GL(X)$ and $\rho^Y : Y \rightarrow GL(Y)$ are representations of G on X and Y . Invariance is a special case of equivariance in which ρ^Y is the trivial representation.

The tensor basis method mentioned in Sect. 2.1 ensures the equivariance of the model by representing tensor functions as linear combinations of Cartesian tensors. Unfortunately, as discussed before, determining the basis tensors can be extremely difficult, with current applications relying on extensive research into the enumeration of bases for second- and third order tensors with particular symmetries [14, 19, 20]. ENNs provide an alternative means to enforce equivariance, and as will be shown shortly, this can be done in a way that guarantees additional tensor relationships via hard constraints in the learning framework.

4.3 Equivariant neural networks

The ENNs considered here use steerable vector spaces to inform the design of equivariant layers. A general recipe for building an equivariant layer ϕ is the following:

1. Define the input and output spaces of the layer, say X and Y , respectively.
2. Specify the representations ρ^X on X and ρ^Y on Y .

3. Ensure ϕ satisfies the equivariance constraint $\rho^Y \circ \phi = \phi \circ \rho^X$.

Step 1 is the same as would be necessary in a traditional neural network, while Steps 2 and 3 introduce the additional structure that constrains the network to be equivariant. The irreducible representations of a group represent the fundamental building blocks of all representations, so they can be used to specify X , Y , ρ^X , and ρ^Y in the above framework. It can be shown that irreducible representations of $O(3)$ are $(2\ell + 1)$ -dimensional and can be indexed by their order $\ell \in \{0, 1, \dots\}$ and their parity p , which can be even ($p = 1$) or odd ($p = -1$).

Let the input space of an equivariant layer be

$$X = \bigoplus_i V_{\ell_i},$$

where V_{ℓ_i} is a steerable vector space of dimension $2\ell_i + 1$. As discussed above, there exists a basis for this space such that elements of $O(3)$ act on vectors in the space as

$$\hat{\mathbf{D}}(\mathbf{R}) = \bigoplus_i \hat{\mathbf{D}}^{(\ell_i)}(\mathbf{R}),$$

which is a block-diagonal matrix with blocks of shape $(2\ell_i + 1) \times (2\ell_i + 1)$. A vector $\mathbf{x} \in X$ can be viewed as a concatenation of spherical tensors $\mathbf{x}^{(\ell_i)} \in V_{\ell_i}$, each of which has $(2\ell_i + 1)$ components $x_m^{(\ell_i)}$, where $-\ell_i \leq m \leq \ell_i$ (The parities p_i are suppressed for clarity).

An expressive way to interact two spherical tensors $\mathbf{x}^{(\ell_1)}$ and $\mathbf{y}^{(\ell_2)}$ is via the Clebsch-Gordon tensor product \otimes_{cg}^w , which is a bilinear, equivariant operation. It is defined by

$$(\mathbf{x}^{(\ell_1)} \otimes_{\text{cg}}^w \mathbf{y}^{(\ell_2)})^{(\ell_3)} = w \sum_{m_1=-\ell_1}^{\ell_1} \sum_{m_2=-\ell_2}^{\ell_2} C_{(\ell_1, m_1)(\ell_2, m_2)}^{(\ell_3, m_3)} x_{m_1}^{(\ell_1)} x_{m_2}^{(\ell_2)}, \quad (13)$$

where $C_{(\ell_1, m_1)(\ell_2, m_2)}^{(\ell_3, m_3)}$ are the Clebsch-Gordon coefficients and w is a single learnable scalar weight. The Clebsch-Gordon coefficients are only nonzero when the types (ℓ_1, ℓ_2, ℓ_3) satisfy the selection rule $|\ell_1 - \ell_2| \leq \ell_3 \leq \ell_1 + \ell_2$. Each viable triple (ℓ_1, ℓ_2, ℓ_3) is often called a path [55], and Eq. 13 is written for a single such path. The input of spherical tensors to the Clebsch-Gordon tensor product can be parts of the same input vector (recall that an input vector is a concatenation of multiple spherical tensors) or two different input vectors. In either case, typically many pairs of spherical tensors can be combined in the product, each pair generally producing several output tensors according to the selection rules.

The output space of the layer is defined similarly to the input space as

$$Y = \bigoplus_i V_{\ell_i},$$

where V_{ℓ_i} are some subset of steerable vector spaces assigned by the tensor product. That is, the output $(\mathbf{x}^{(\ell_1)} \otimes_{\text{cg}}^w \mathbf{y}^{(\ell_2)})^{\ell_3}$ of each path is a steerable vector belonging to some V_{ℓ_i} , and one may choose which subset of these to concatenate into an output vector $\mathbf{y} \in Y$, typically by fixing a maximum frequency ℓ_{max} . In this work, the nonlinear gating mechanism of [27] is applied to the output \mathbf{y} , and the result is used as input to the next layer. In this way, working with irreducible representations facilitates the design of modular layers suitable for a neural network.

4.4 Enforcing tensor constraints

It is possible to enforce at least three distinct types of tensor constraint in the architecture of an ENN:

1. Equivariance
2. Index permutation symmetries
3. Linear constraints

The first of these is enforced by constructing the network as a composition of only equivariant functions, for example the Clebsch-Gordon tensor product and equivariant gate discussed in Sec. 4.3. Although implied by the name, it is included in the above list to make clear the fact that these are indeed separate types of constraint, in the sense that enforcing one does not automatically enforce the others.

4.4.1 Index permutation symmetries

It is common for certain components of a tensor to always be equal (or related by a minus sign), either by definition or as a consequence of physical symmetry. Such constraints are usually specified with a statement like $T_{ij} = T_{ji}$ or $T_{ij} = -T_{ji}$, which states that a second-order tensor \mathbf{T} is symmetric or antisymmetric, respectively. The set of symmetry operations on the tensor indices constitutes a permutation group G .

Viewing the space of all possible tensor components as a vector space V , one can write down a representation ρ_p of G as a set of permutation matrices with dimension equal to the number of possible tensor components. These matrices describe how the tensor components permute under a symmetry operation on the indices. As with any finite-dimensional representation, ρ_p can be decomposed into irreducible representations. One may also write down a one-dimensional, and hence irreducible, representation ρ_s that stores only the signs associated with each index permutation.

A key result from representation theory is that for any finite group G with representation ρ , the operator

$$\mathbf{P}_j = \frac{\ell_j}{|G|} \sum_{g \in G} \chi_{\rho_j}(g)^* \rho(g), \quad (14)$$

where $*$ denotes complex conjugation, is a projection operator onto the subspace that transforms as the irreducible representation ρ_j . Here, ℓ_j and χ_{ρ_j} are the dimension and character, respectively, of ρ_j . The projector \mathbf{P}_s , obtained by taking $\rho_j = \rho_s$, projects vectors in the space V of all possible tensor components into a subspace $V_s \subseteq V$ with dimension equal to the true number of degrees of freedom in the tensor after removing those fixed by index permutation symmetry.

Sec. 4.1 explained how the vector space V , carrying a representation ρ , can be decomposed into irreducible subspaces. The same can be done for the subspace V_s , which carries a representation π containing a subset of the irreducible subspaces in ρ . Just as one could solve Eq. 11 with ρ to obtain \mathbf{S}_ρ in Eq. 12, the same can be done using $\pi = \mathbf{P}_s \rho \mathbf{P}_s^T$ to obtain \mathbf{S}_π . The transformation that expresses a flattened tensor $\text{vec}(\mathbf{T})$ in the spherical basis, accounting for index permutation symmetries, is therefore $\mathbf{S}_\pi \mathbf{P}_s$ ⁹. One can use an ENN to output components in the subspace

⁹It is important to note that, because of their reference to π and ρ , respectively, \mathbf{S}_π and \mathbf{P}_s depend on the tensor being considered. If different instances of these matrices appear in the same equation, they will be explicitly distinguished, but otherwise, it should be understood that they represent the realization appropriate to the tensor they transform.

V_s and transform back to V to obtain predictions satisfying index permutation symmetries. An implementation of this is available in the `CartesianTensor` class of the `e3nn` library [55].

4.4.2 Linear tensor constraints

In this section, a novel algorithm and ENN layer are introduced that can exactly enforce linear tensor constraints on top of equivariance and index permutation symmetries. Linear tensor constraints arise in relationships that involve contractions of one or more pairs of indices of a tensor, for example the condition that a tensor be trace-free (In the language of many deep learning libraries, these could be called “Einsum”-style constraints).

As motivation for the procedure, consider again the example of a second-order tensor \mathbf{T} . One can see from Fig. 1 that if \mathbf{T} is symmetric, the components of the $\ell = 1$ subspace are all identically zero, so these three degrees of freedom are fixed. Since this constraint arises due to an index permutation symmetry, it is taken care of by the projection operator \mathbf{P}_s from Sec. 4.4.1 and does not need to be identified manually. However, the idea of looking for physically meaningful component patterns on the spherical basis underlies the method for enforcing linear constraints.

In particular, note that the component of the irreducible representation $\ell = 0$ is precisely the trace. All one must do to make a trace-free prediction for \mathbf{T} is to set $T_0^{(0,p)} = 0$ in the spherical basis before transforming back to the Cartesian basis. However, this example represents a convenient special case: since the irreducible representation $\ell = 0$ is one-dimensional, *any* change of basis \mathbf{S}_ρ in the spherical basis makes this component easily identifiable as the trace. If linear constraints involve higher-dimensional subspaces, in which indefinitely many choices are available for the basis (beyond scaling), a more systematic approach is needed to identify the appropriate components to fix in the spherical basis.

To this end, suppose that \mathbf{T} is an n th-order tensor that satisfies one or more linear constraints such as $T_{ijkk} = K_{ij}^{(1)}$ or $\varepsilon_{ijk}T_{klm} = K_{ijlm}^{(2)}$ for some Cartesian tensors $\mathbf{K}^{(1)}$ and $\mathbf{K}^{(2)}$. Each constraint may be written as $\mathbf{\Lambda}^{(i)} \text{vec}(\mathbf{T}) = \text{vec}(\mathbf{K}^{(i)})$ for some constant matrix $\mathbf{\Lambda}^{(i)}$, where each row of $\mathbf{\Lambda}^{(i)}$ encodes one component of the relation. For example, if \mathbf{T} is a second-order symmetric tensor, the row representing a trace-free constraint would be $(1, 0, 0, 0, 1, 0, 0, 0, 1)$. Importantly, if \mathbf{T} is a tensor function, the prescribed values $\mathbf{K}^{(i)}$ may depend on the input.

Since each $\mathbf{K}^{(i)}$ is a Cartesian tensor, possibly with its own index permutation symmetries, its components may be decomposed via left multiplication by $\mathbf{S}_\pi \mathbf{P}_s$ (see the footnote in Sec. 4.4.1). Using this, the constraint equation can be written as

$$\hat{\mathbf{\Lambda}}^{(i)} \text{vec}(\mathbf{T}) = \mathbf{S}_\pi \mathbf{P}_s \text{vec}(\mathbf{K}^{(i)}), \quad (15)$$

where $\hat{\mathbf{\Lambda}}^{(i)} = \mathbf{S}_\pi \mathbf{P}_s \mathbf{\Lambda}^{(i)}$. All the tensor constraints can be collected into a single statement

$$\hat{\mathbf{\Lambda}} \text{vec}(\mathbf{T}) = \text{vec}(\mathbf{K})$$

by stacking the rows of $\hat{\mathbf{\Lambda}}^{(i)}$ and the right-hand side of Eq. 15 for all i .

The key observation is that, since each $\mathbf{K}^{(i)}$ can be decomposed into irreducible representations, there exists a particular choice of spherical bases in which the component values are known. What is needed is to find a common set of bases for the subspaces produced by 1) decomposing \mathbf{T} into irreducible representations and 2) decomposing the tensors generated via contraction, e.g. T_{ijkk} or $\varepsilon_{ijk}T_{klm}$, into irreducible representations. Then it becomes clear which components of \mathbf{T} are fixed by linear constraints and which degrees of freedom remain to be predicted.

Alg. 1 specifies a procedure for computing a matrix \mathbf{E} that performs this basis alignment. Specifically, it returns \mathbf{E} , $\boldsymbol{\alpha}$, and $\boldsymbol{\beta}$ such that the components of

$$\tilde{\mathbf{T}} = \mathbf{E}^T \mathbf{S}_\pi \mathbf{P}_s \text{vec}(\mathbf{T})$$

Algorithm 1: Linear constraint alignment matrix

at indices α equal the components of $\text{vec}(\mathbf{K})$ at indices β , that is, $\tilde{\mathbf{T}}[\alpha] = \text{vec}(\mathbf{K})[\beta]$. In practice, one predicts the components of $\tilde{\mathbf{T}}$ at the indices not in α , fills in the remaining components by setting $\tilde{\mathbf{T}}[\alpha] = \text{vec}(\mathbf{K})[\beta]$, and applies the inverse transformation $\mathbf{P}_s^T \mathbf{S}_\pi^{-1} (\mathbf{E}^T)^{-1} \tilde{\mathbf{T}}$ to produce a tensor in the Cartesian basis that satisfies the constraints, as shown in Stage 3 of Fig. 2.

The following details accompany the indicated line numbers from Alg. 1:

- Input: The index permutation symmetries of \mathbf{T} determine \mathbf{P}_s , which is used to construct the representation $\pi = \mathbf{P}_s \rho \mathbf{P}_s^T$ that acts on V_s . Eq. 11 is solved for increasing values of ℓ to find a list of solutions $\{\mathbf{S}_\pi^{(\ell_i)}\}$ with dimensions $\{\ell_i\}$ until the cumulative dimension of the solutions equals the dimension of V_s . Importantly, the rows of $\hat{\mathbf{\Lambda}}$ should be made linearly independent so that \mathbf{E} is invertible (see App. 8.6).
- Line 6: The number of columns of $\hat{\mathbf{\Lambda}}$ is equal to the number of components of \mathbf{T} (That is, each row represents a constraint and is specified with respect to V , the space of all tensor components). To express the rows with respect to V_s , and thereby account for index permutation symmetries, the projector \mathbf{P}_s must act on the columns of $\hat{\mathbf{\Lambda}}$, hence the transposition.
- Lines 11-15: $\text{LeastSquares}(\mathbf{A}^T, \mathbf{B})$ denotes a batched least squares problem, in which a solution is sought for each column of \mathbf{B} independently. If the residual is zero for any of the columns, the spherical basis at order ℓ spans a space in which components of the linear constraints live. The solutions corresponding to zero-residual columns relate the spherical and constraint bases, providing the desired mapping needed to equate components.

Formally, Alg. 1 accounts for the fact that the decomposition of an isotypic component of a group representation is not unique¹⁰. If the multiplicity of an order- ℓ irreducible representation is k , the representation matrices on this isotypic component can be written as $\mathbf{I}_k \otimes_{\text{kr}} \hat{\mathbf{D}}^{(\ell)}(\mathbf{R})$. Schur’s lemma requires that a change of basis in this subspace must be of the form $\mathbf{U} = \mathbf{U}_k \otimes_{\text{kr}} \mathbf{I}_{2\ell+1}$, where \mathbf{U}_k is any $k \times k$ unitary matrix, showing that there is a $U(k)$ freedom to “mix” the k copies of the order- ℓ irreducible representations amongst themselves¹¹. Alg. 1 determines whether two isotypic components are expressed differently under this freedom and provides a map to align them.

4.5 Architecture

An overview of the complete ENN architecture used here is shown in Fig. 2. In Stage 1 of the network, Cartesian tensors are decomposed via left multiplication by the matrix $\mathbf{S}_\pi \mathbf{P}_s$ appropriate to each input tensor. Stage 2 contains a sequence of L equivariant MLP layers, where $\otimes_{\text{cg}}^{\mathbf{W}}$ denotes the fully-connected Clebsh-Gordon tensor product of the hidden representation and the original input¹². Intermediate layers consist of even and odd parity irreducible representations for orders up to and including $\ell_{\max} = 6$, with multiplicities chosen such that each order has roughly the same number of components [27].

The different types of tensor constraints described in Sec. 4.4 are enforced via single matrix multiplications at the encoding and decoding stages of the network and hence represent lightweight modifications relative to the processing block. Additionally, the matrices involved need be computed only once offline. Stage 3 of the figure shows the novel output head, in which predictions from the ENN are concatenated with constraint-determined component values in a common spherical basis before being decoded in Stage 4 back into the Cartesian space.

The architecture is implemented with PyTorch using the `e3nn` library [55]. As the new layer operates on the output of the MLP blocks, it has the advantage that no code changes to the library are required.

5 Results

In this section, experiments are shown for RANS closure modeling in RDT, using the framework advanced by Kassinos and Reynolds [7, 50]. Across the three closure modeling problems required in this setting, there are 405 total tensor components that must be predicted. Exploiting the strategies in Sec. 4.4, only 47 of these need to be predicted independently. The constraints governing the remaining 88% are enforced exactly, regardless of training.

5.1 Modeling objective

The system of Eqs. 6-8 requires closure models to be obtained for

$$\mathbf{M}(\langle u_i u_j \rangle, \mathbf{D}, \mathbf{Q}^*), \quad \mathbf{L}(\mathbf{D}, \mathbf{Q}^*), \quad \text{and} \quad \mathbf{J}(\langle u_i u_j \rangle, \mathbf{D}, \mathbf{Q}^*). \quad (16)$$

Several considerations help frame the problem:

¹⁰An isotypic component of a representation is the direct sum of all irreducible subspaces transforming according to a specific irreducible representation ℓ , or intuitively the number of “copies” of a particular irreducible representation that appear within a larger representation.

¹¹The freedom is $U(k)$, the unitary group of degree k , assuming \mathbf{U}_k maps between orthonormal bases. If this is not the case, \mathbf{U}_k can belong to a larger group of matrices.

¹²Fully-connected refers to the terminology used to describe the `FullyConnectedTensorProduct` class of the `e3nn` library [55]. The bold \mathbf{W} denotes the collection of weights for all paths, in contrast to the scalar w in Eq. 13, which is written for a single path

	Order	Index permutation symmetry
M	4	$M_{ijpq} = M_{ijqp} = M_{jipq} = M_{jiqp}$
M*	4	Fully symmetric
L	4	Fully symmetric
$\langle u_i u_j \rangle$	2	Fully symmetric
D	2	Fully symmetric
Q	3	No symmetry
Q*	3	Fully symmetric
J	5	$J_{ijrpq} = J_{ijrqp} = J_{ijprq}$ $= J_{ijpqr} = J_{ijqrp} = J_{ijqpr}$

Table 1: Tensor symmetries [7].

		Constraints
M		$M_{ikkj} = 0$
		$M_{ijkk} = \langle u_i u_j \rangle$
		$M_{kkij} = D_{ij}$
		$\text{Sym}(\varepsilon_{ipq} M_{jqp}) = Q_{ijk}^*$
M*		$M_{ijkk} = \frac{1}{6}(\langle u_i u_j \rangle + D_{ij})$
L		$L_{ijkk} = D_{ij}$
J		$J_{kkijr} = 0$
		$J_{ikjrk} = 0$
		$J_{kijrk} = 0$
		$\varepsilon_{jsr} J_{sirkk} = \langle u_i u_j \rangle$
		$\varepsilon_{irs} J_{srjkk} = D_{ij}$
		$\text{Sym}(J_{ijrkk}) = Q_{ijr}^*$

Table 2: Modeling constraints [7].

- The learned models implicitly form higher-order polynomials of the tensors. To ensure that these models are consistent with dimensional analysis, all tensors in Eq. 16 are normalized by the turbulent kinetic energy.
- All quantities shown are (generalized) Cartesian tensors, so their components must satisfy the implied transformation rules, namely Eq. 9 on the Cartesian basis or Eq. 10 on the spherical basis. This is the core principle that motivates the use of ENNs.
- Any other structural constraints should also be respected. That is, the outputs should satisfy the index permutation symmetries listed in Tab. 1.
- Known physical constraints should be satisfied. The relevant constraints for this case are shown in Tab. 2.
- The functions in Eq. 16 are local in the sense that they relate quantities at a single position and time. In an inhomogeneous flow, one might consider a dependence on values in a neighborhood instead.

The three middle considerations illustrate why each of the three properties discussed in Sect. 4.4 is relevant to RANS modeling. Importantly, *all of the constraints in Tabs. 1 and 2 are enforced exactly by the network architecture* and so are obeyed regardless of training, in contrast to the soft constraint strategies mentioned in Sec. 2.3.

5.2 Data generation

A data set for this RDT problem is a collection of data points and targets at N space-time locations, where the k th data point consists of an input tuple $(\langle u_i u_j \rangle_k, \mathbf{D}_k, \mathbf{Q}_k^*)$, and the corresponding target is one of \mathbf{M}_k , \mathbf{L}_k , or \mathbf{J}_k depending on the closure sought. Once this data set is obtained, the training procedure can follow a standard supervised learning design. The loss function used here is the mean-squared error between the ENN predictions and the targets, which can be measured on either a spherical basis or a Cartesian basis.

The definition of \mathbf{M} is given in Eq. 5, while the other inputs and targets may be defined as

$$D_{ij} \equiv \iiint_{-\infty}^{\infty} \Phi_{nn} \frac{\kappa_i \kappa_j}{\kappa^2} d\kappa \quad \text{and} \quad \mathbf{Q}^* \equiv \text{Sym}(\mathbf{Q}), \quad Q_{ijk} \equiv \varepsilon_{ipq} \iiint_{-\infty}^{\infty} \Phi_{jq} \frac{\kappa_p \kappa_k}{\kappa^2} d\kappa \quad (17)$$

and

$$L_{ijkl} \equiv \iiint_{-\infty}^{\infty} \Phi_{nn} \frac{\kappa_i \kappa_j \kappa_k \kappa_l}{\kappa^4} d\kappa \quad \text{and} \quad J_{ijrpq} \equiv \varepsilon_{its} \iiint_{-\infty}^{\infty} \Phi_{sj} \frac{\kappa_t \kappa_r \kappa_p \kappa_q}{\kappa^4} d\kappa, \quad (18)$$

respectively. Using these definitions, all of the necessary data may be generated from the velocity spectrum tensor Φ by integrating over wavevector space. The velocity spectrum tensor, following a particular wavevector $\kappa(t)$, evolves from an initial condition $\Phi(0)$ according to

$$\frac{d\Phi_{ij}}{dt} = -\frac{\partial \langle U_i \rangle}{\partial x_k} \Phi_{kj} - \frac{\partial \langle U_j \rangle}{\partial x_k} \Phi_{ik} + 2 \frac{\partial \langle U_\ell \rangle}{\partial x_k} \left(\frac{\kappa_i \kappa_\ell}{\kappa^2} \Phi_{kj} + \frac{\kappa_j \kappa_\ell}{\kappa^2} \Phi_{ik} \right), \quad (19)$$

where the wavevector itself evolves from an initial condition $\kappa(0)$ according to

$$\frac{d\kappa_\ell}{dt} = -\kappa_j \frac{\partial \langle U_j \rangle}{\partial x_\ell}.$$

Eq. 19 cannot be solved for every wavevector, so an alternative procedure is applied using solutions for wavevectors initially distributed on the unit sphere (See Fig. 3). The initial shell of wavevectors distorts with time, but a change-of-variables allows integrals over the surface to be mapped back to the sphere. As long as the initial condition for Φ does not depend on wavevector magnitude, the solutions are separable into magnitude-dependent and direction-dependent parts, such that the integrals in Eqs. 5, 17, and 18 can all be evaluated by weighted integrals over spherical shells.

Data is generated for 320 different mean velocity gradients, sampled using Sobol sequencing [56], by integrating Eq. 19 along wavevectors initially distributed at 6,051 spherical design points, which are equal-weight numerical quadrature points that guarantee exact integration on the unit sphere for spherical polynomials up to a certain degree (here, ≤ 109) [57]. Storing Φ at 100 time steps per simulation, this procedure produces 32,000 samples for each closure problem.

5.3 ENN training and evaluation

First, results are presented for the modeling of $\mathbf{M}^*(\langle u_i u_j \rangle, \mathbf{D})$ and $\mathbf{M}(\langle u_i u_j \rangle, \mathbf{D}, \mathbf{Q}^*)$, where \mathbf{M}^* is the fully symmetric part of \mathbf{M} . A tensor basis for $\langle u_i u_j \rangle$ and \mathbf{D} is known, as is a decomposition of \mathbf{M} in terms of \mathbf{M}^* , so the ENN approach can be fairly compared to the TBM when modeling $\mathbf{M}^*(\langle u_i u_j \rangle, \mathbf{D})$. The purpose of modeling $\mathbf{M}(\langle u_i u_j \rangle, \mathbf{D}, \mathbf{Q}^*)$ is to investigate the effect of adding dependence on \mathbf{Q}^* , which only the ENN can accommodate. Analogously, results are shown for models of $\mathbf{L}(\mathbf{D})$ and $\mathbf{L}(\mathbf{D}, \mathbf{Q}^*)$, where the former allows direct comparison with the TBM. As baselines are not available for \mathbf{J} , trained models for this quantity are not shown. Instead, this case is used to illustrate the role of the \mathbf{E} matrix produced by Alg. 1.

The **e3nn** shorthand “ $m_1 \times \ell_1 p_1 + m_2 \times \ell_2 p_2 + \dots$ ” is used in this section to describe spherical tensors, where m_i , ℓ_i , and p_i denote the multiplicity, order, and parity, respectively, of the irreducible representations that make up a tensor¹³. For example, $3 \times 0e + 2e$ denotes a spherical tensor that is the direct sum of three irreducible representations $\ell = 0$ and one irreducible representation $\ell = 2$, all of even parity.

As mentioned in Sect. 5.2, the complete data set consists of 32,000 samples from 320 independent simulations. All models are trained on 40% of this data, chosen by sampling 128 simulations and

¹³Examples of this notation are available in the **e3nn** documentation at <https://docs.e3nn.org/>.

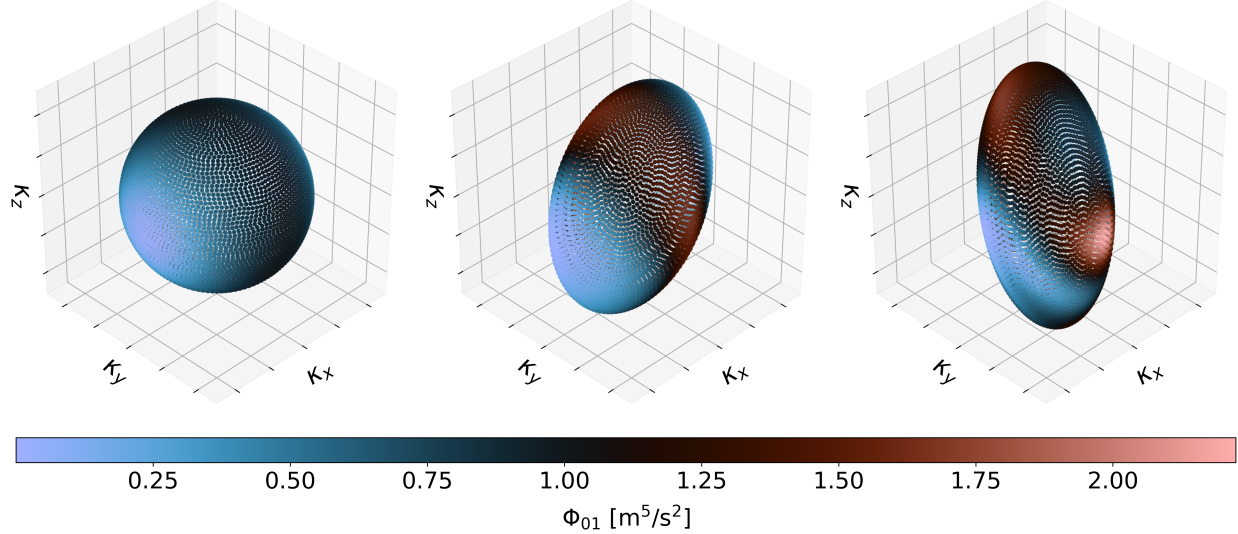


Figure 3: Evolution of wavevectors $\kappa(t)$ at which the velocity spectrum tensor Φ can be integrated independently. Each marker corresponds to a wavevector, initially located at a spherical design quadrature point on the unit sphere. As time proceeds (left to right in the figure), the wavevectors distort, and the values of Φ following the wavevectors evolve.

including all 100 time steps from each. Although viewing the 32,000 samples as a single pool would lead to a more diverse data set, the previous method is preferred because it guarantees that the validation and test sets consist of velocity gradients that have not been seen during training. The decision was made to use a relatively small fraction of the data for training to keep training times low while using a small batch size (The batch size used was 32). The batch size was observed to be one of the most critical hyperparameters, with lower batch sizes leading to better performance. Additional details regarding training and hyperparameters can be found in App. 8.2.

5.3.1 Modeling \mathbf{M}

It is shown in [50] that \mathbf{M} satisfies the exact decomposition

$$\begin{aligned}
 M_{ijkl} = & M_{ijkl}^* \\
 & + \frac{1}{2}(\varepsilon_{zkl}Q_{zil}^* - \varepsilon_{zil}Q_{zkl}^*) \\
 & + \frac{1}{6}[(\delta_{il}\delta_{jk} + \delta_{ik}\delta_{lj} - 2\delta_{ik}\delta_{jl})q^2 + 3(\delta_{kl}\langle u_i u_j \rangle + \delta_{ij}D_{kl}) + \delta_{kl}D_{ij} + \delta_{ij}\langle u_k u_l \rangle \\
 & - \delta_{il}(\langle u_k u_j \rangle + D_{kj}) - \delta_{kj}(\langle u_i u_l \rangle + D_{il}) - \delta_{ik}(\langle u_l u_j \rangle + D_{lj}) - \delta_{lj}(\langle u_k u_i \rangle + D_{ki})],
 \end{aligned} \tag{20}$$

so one can either model \mathbf{M} directly or model \mathbf{M}^* and use this decomposition to construct \mathbf{M} . In the most general case, either model would include all of $\langle u_i u_j \rangle$, \mathbf{D} , and \mathbf{Q}^* as dependencies. A tensor basis that includes \mathbf{Q}^* is not known, so the most expressive approach allowed by the TBM is to model $\mathbf{M}^*(\langle u_i u_j \rangle, \mathbf{D})$ and include \mathbf{Q}^* dependence only through the linear terms in Eq. 20.

Under the symmetries in Tab. 1, \mathbf{M} decomposes into a $2 \times 0e + 1e + 3 \times 2e + 3e + 4e$ spherical tensor with 36 components. The constraints in Tab. 2 fix the components for $\ell \in \{0, 1, 2, 3\}$, leaving only the nine $\ell = 4$ components to be predicted. The \mathbf{M}^* tensor decomposes into $0e + 2e + 4e$, a spherical tensor with 15 components. Of these, the components of the $\ell = 0$ and $\ell = 2$ irreducible

representations are fixed. It is shown in App. 8.5 how the relations in Tab. 2 for \mathbf{M} , which correspond to 27 independent constraints, translate into six independent constraints for \mathbf{M}^* .

As mentioned in Sec. 5.2, the training procedure for all closure models follows a supervised learning design, and the predicted and target tensors may be compared in either the spherical or Cartesian bases. The former requires less computation and raises a consideration related to the ability to exactly enforce constraints.

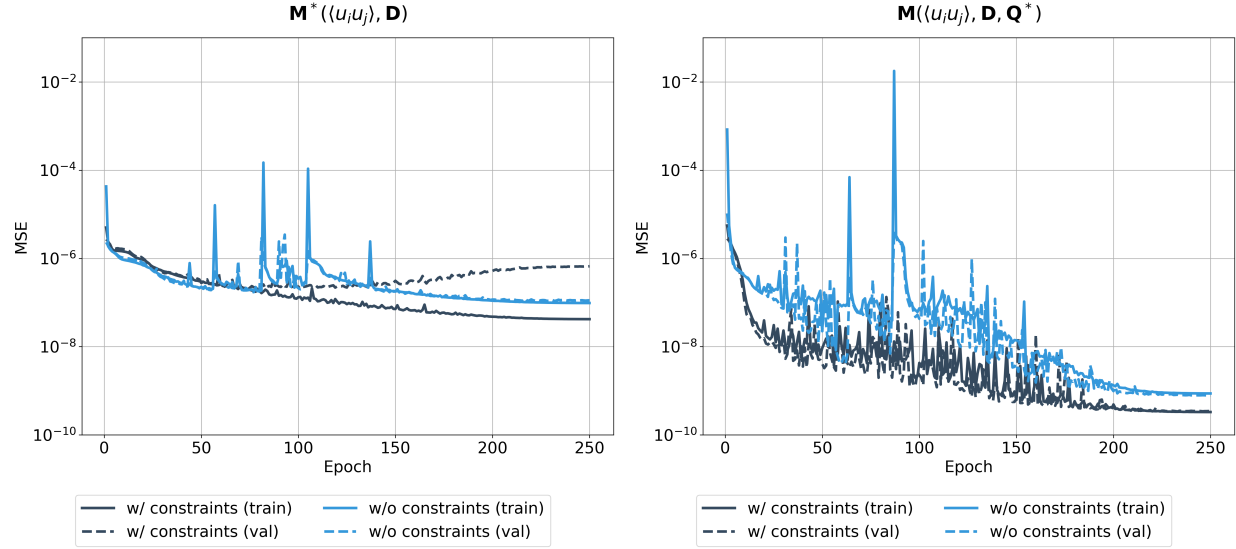


Figure 4: ENN training and validation loss when learning \mathbf{M}^* (left) and \mathbf{M} (right) with and without the constraints in Tab. 2 enforced. “W/ constraints” refers to learning with supervision from only the nine components of the $\ell = 4$ irreducible representation, while “w/o constraints” refers to supervising on all 15 components of the $0e + 2e + 4e$ spherical tensor.

While all constraints should undoubtedly be enforced at inference time to guarantee physically valid predictions, this does not necessarily mean that they should be enforced during training. Note that for both \mathbf{M}^* and \mathbf{M} , the only unconstrained components are those of the $\ell = 4$ irreducible representation. If the ENN is made to predict only these components, the gradient signal during training will come entirely from the highest frequency part of the tensor, which may make the network more prone to find spurious features relevant only to the $4e$ components.

Alternatively, learning to predict the components of all the irreducible representations, including those fixed by the constraints, may serve as a source of implicit regularization. The argument for this is that the predictions for each order ℓ rely on the same shared internal representation up until the final network layer. Hence, the learned internal features must be versatile enough to benefit all tasks, discouraging learning pathways that overfit to the $4e$ components.

In practice, it was observed that keeping known components in the training loss could avoid overfitting when an identical model trained on only unknown components did overfit (The reverse was not observed). For example, Fig. 4 shows the results of learning \mathbf{M}^* and \mathbf{M} with supervision on only the $4e$ components of the spherical tensors versus on all of the components. For \mathbf{M}^* , enforcing the constraints during training leads to overfitting, evidenced by the divergence of the training and validation curves. Alternatively, when supervising on all components, the training and validation curves track one another well. Still, either supervision approach leads to overfitting with enough parameters, and this behavior may not hold for different learning rates.

In the baseline comparisons, to avoid presenting results that may benefit from overfitting, the

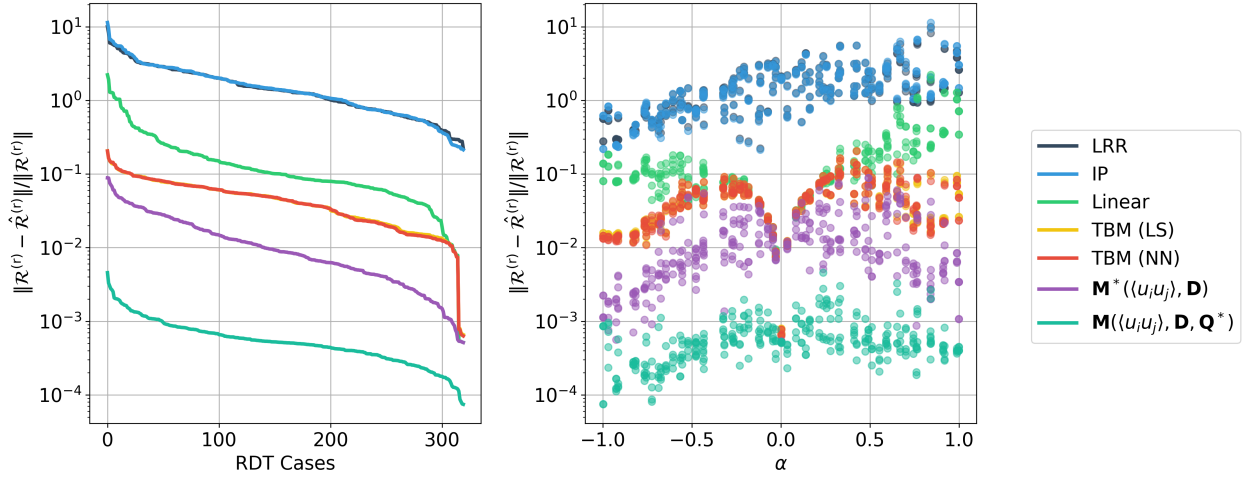


Figure 5: Error in predictions of the rapid pressure-rate-of-strain-tensor $\mathcal{R}_{ij}^{(r)}$. Left: Errors listed in decreasing order. Right. Errors ordered by amount of strain, with $|\alpha| = 1$ representing pure strain and $|\alpha| = 0$ representing pure rotation. The LRR and IP curves nearly overlap, as do the two TBM curves.

\mathbf{M}^* model trained on all components is used. For \mathbf{M} , the training and validation curves track one another well in either supervision case. Since the model trained with constraints performs better without overfitting, this is the one used in the baseline comparisons.

Fig. 5 shows comparisons of ENN models for $\mathbf{M}(\langle u_i u_j \rangle, \mathbf{D}, \mathbf{Q}^*)$ and $\mathbf{M}^*(\langle u_i u_j \rangle, \mathbf{D})$ to the tensor basis method and several analytical baselines. The vertical axis measures relative error in the rapid pressure-rate-of-strain tensor $\mathcal{R}_{ij}^{(r)}$, which is related to \mathbf{M} via

$$\mathcal{R}_{ij}^{(r)} = 2 \frac{\partial \langle U_n \rangle}{\partial x_m} (M_{imnj} + M_{jmni}),$$

the final term appearing on the right-hand-side of Eq. 6.

The ENN model for $\mathbf{M}^*(\langle u_i u_j \rangle, \mathbf{D})$ is shown to provide a fair comparison to the TBM. For both \mathbf{M}^* models, \mathbf{Q}^* is excluded as an input, and the decomposition in Eq. 20 is used to complete the model for \mathbf{M} . The distinction between LS and NN in the legend refers to whether the TBM coefficients are constants, determined by least squares (LS), or functions of the tensor invariants, parameterized by a neural network (NN) as in [11].

The ENN model for $\mathbf{M}(\langle u_i u_j \rangle, \mathbf{D}, \mathbf{Q}^*)$ is shown to investigate the effect of adding general nonlinear \mathbf{Q}^* dependence. While the general model could be built by learning $\mathbf{M}^*(\langle u_i u_j \rangle, \mathbf{D}, \mathbf{Q}^*)$ and using Eq. 20, directly learning \mathbf{M} reflects the motivation of the ENN approach, which is to mitigate reliance on a priori tensor analysis. It turns out, though, that when supervising only on the unconstrained spherical components, that the distinction between learning \mathbf{M} and \mathbf{M}^* disappears. The reason is that, in both cases, the only components to be learned are those of the $\ell = 4$ irreducible representation, and these are identical for \mathbf{M} and \mathbf{M}^* provided that no term in Eq. 20 other than \mathbf{M}^* contains an $\ell = 4$ component.

Indeed, the $\ell = 4$ term of a fourth-order tensor decomposition corresponds to the fully symmetric trace-free (STF) component, to which none of the remaining terms can contribute. For the terms involving the Levi-Civita symbol, the contraction creates an antisymmetric pair of indices, which vanish under full symmetrization. For the others, the presence of at least one pair of free indices over the Kronecker delta means that these terms will generally have nonzero trace and vanish in an

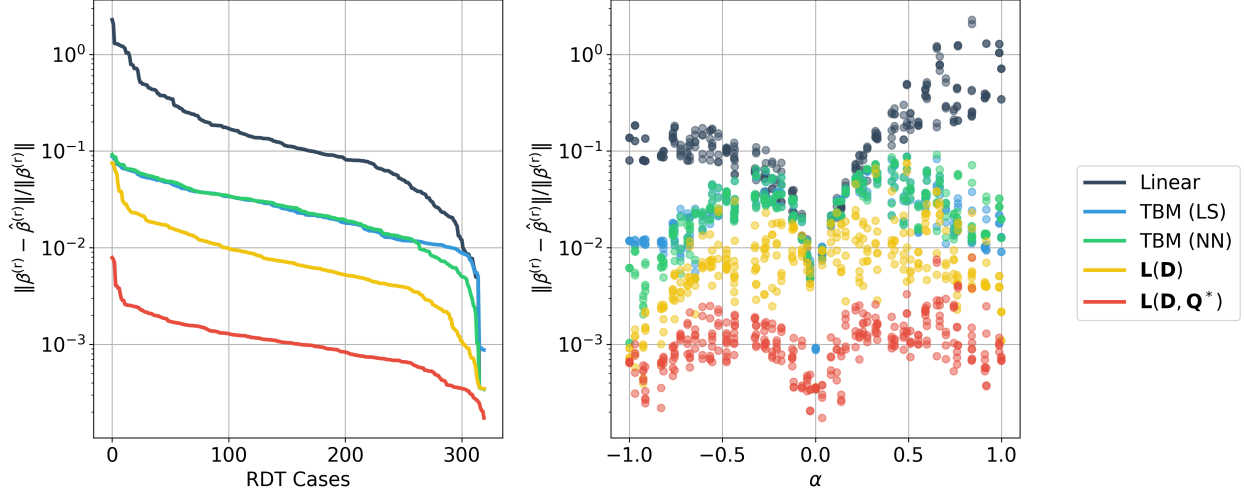


Figure 6: Error in predictions of $\beta_{ij}^{(r)}$. Left: Errors listed in decreasing order. Right. Errors ordered by amount of strain (See Fig. 5).

STF projection. An alternative, representation theory perspective is that the terms other than \mathbf{M}^* consist of either the Levi-Civita symbol or the Kronecker delta, which are 0e and 0e, respectively, coupled with one other tensor having at most an $\ell = 3$ component.

The analytical baselines shown in the figure are the linear model of [50] (Linear), as well as the Launder-Reece-Rodi [58] (LRR) and the isotropization of the production models [59] (IP).

5.3.2 Modeling \mathbf{L}

The \mathbf{L} tensor decomposes into irreducible representations 0e + 2e + 4e, the same as in \mathbf{M}^* . The supervision of all or only the unknown components of the irreducible representations was found to make a negligible difference when predicting \mathbf{L} , both as a function of \mathbf{D} and as a function of \mathbf{D} and \mathbf{Q}^* . The reported models were arbitrarily chosen to be those trained when supervising only the unknowns.

Fig. 6 shows the performance of ENN models for $\mathbf{L}(\mathbf{D})$ and $\mathbf{L}(\mathbf{D}, \mathbf{Q}^*)$ for predicting

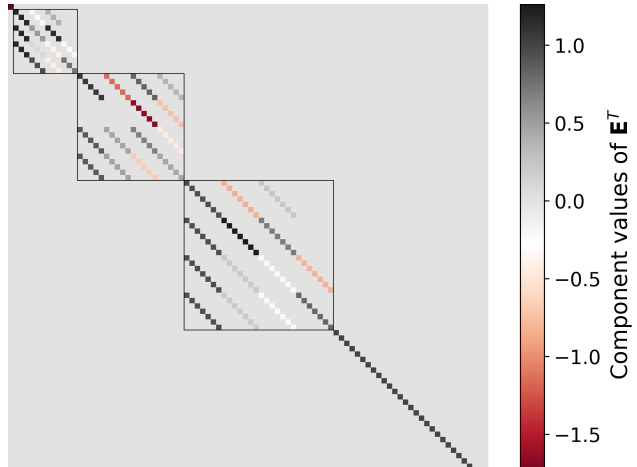
$$\beta_{ij}^{(r)} = 2 \frac{\partial \langle U_m \rangle}{\partial x_n} (L_{imnj} - M_{mni}), \quad (21)$$

which is the final term of Eq. 7. For the \mathbf{M} term in Eq. 21, models from Sec. 5.3.1 are used instead of the ground truth for both the ENN and TBM, reflecting the fact that closures for \mathbf{L} and \mathbf{M} must be used together in practice. The $\mathbf{L}(\mathbf{D})$ model is paired with the $\mathbf{M}^*(\langle u_i u_j \rangle, \mathbf{D})$ model to admit fair comparison to the TBM, which does not allow include \mathbf{Q}^* dependence outside the linear terms in Eq. 20. The $\mathbf{L}(\mathbf{D}, \mathbf{Q}^*)$ model is paired with the $\mathbf{M}^*(\langle u_i u_j \rangle, \mathbf{D}, \mathbf{Q}^*)$ model.

It can be seen that the ENNs outperform the other methods across the range of mean velocity gradients. The elevated error near $|\alpha| = 0$ (and the error spike on the left plot, which shows the errors in descending order) reflects ill-conditioning in the relative error calculation, as the ground-truth denominator rapidly approaches zero as $|\alpha| \rightarrow 0$. As with modeling \mathbf{M} , inclusion of general \mathbf{Q}^* dependence leads to a clear performance improvement.

Constraint	Irreps.
$J_{kkijr} = 0$	1o + 3o
$J_{ikjrk} = 0$	1o + 2o + 3o
$J_{kijrk} = 0$	1o + 2o + 3o
$\varepsilon_{jsr} J_{sirkk} = \langle u_i u_j \rangle$	0o + 2o
$\varepsilon_{irs} J_{srjkk} = D_{ij}$	0o + 2o
$\text{Sym}(J_{ijrkk}) = Q_{ijr}^*$	1o + 3o

(a) Decomposition of linear constraints into irreducible representations.



(b) \mathbf{E}^T from Alg. 1, computed for decomposing the \mathbf{J} tensor.

Figure 7: The \mathbf{J} tensor decomposes into $0o + 4 \times 1o + 4 \times 2o + 4 \times 3o + 2 \times 4o + 5o$. Of these, all the component values for irreducible representations with $\ell < 4$ are fixed by the constraints in Fig. 7a. When the irreducible representations are ordered by increasing ℓ , as in Fig. 7b, \mathbf{E}^T is block diagonal, with each block representing an isotypic component. Solid lines surround the subspaces for $\ell \in \{0, 1, 2, 3\}$, which are those affected by the constraints.

5.3.3 Modeling \mathbf{J}

As no baselines are available for \mathbf{J} , this section is used to provide more details about the role of \mathbf{E} from Alg. 1.

The \mathbf{J} tensor decomposes into $0o + 4 \times 1o + 4 \times 2o + 4 \times 3o + 2 \times 4o + 5o$ irreducible representations. When $\mathbf{S}_\pi \mathbf{P}_s$ is applied to $\text{vec}(\mathbf{J})$, the Cartesian components of \mathbf{J} are projected into bases that span these irreducible subspaces. The particular bases are determined by the method used to solve Eq. 11. Meanwhile, the constraints on \mathbf{J} can themselves be decomposed into irreducible subspaces, as shown in Fig. 7a. While this decomposition is also achieved by solving Eq. 11 and projecting with $\mathbf{S}_\pi \mathbf{P}_s$, the fact that the components of \mathbf{J} are mixed by a contraction prior to this projection means that the resulting bases will not necessarily be the same. This is a reflection of the fact that isotypic component decompositions are not unique.

The proposed ENN layer corrects for this by using the \mathbf{E} matrix, shown in Fig. 7b, to synchronize the isotypic component decompositions. Solid lines enclose the isotypic components that are affected by constraints. For example, the largest block contains four copies of the $\ell = 3$ irreducible representation. Note that subspaces of a given ℓ are mixed with constant matrices. This is a consequence of Schur’s lemma, provided that the same basis convention is used for each individual subspace, as is the case here.

6 Discussion

This paper introduces ENNs to represent tensor function closures for the tensorial base proposed by Kassinos and Reynolds. The results indicate that the method achieves state-of-the-art performance for RANS modeling in the RDT limit. Using tools from the representation theory of tensors, a novel method was developed to enforce exactly linear tensor constraints alongside equivariance and index

permutation symmetries. Experiments on new RDT data demonstrate that the proposed approach outperforms analytical models and learned models based on tensor basis expansions, achieving up to an order of magnitude decrease in relative error across a wide range of mean velocity gradients. Furthermore, by avoiding the need to derive tensor bases, ENNs enable fast exploration of different model dependencies, demonstrated here by the inclusion of general, nonlinear stropholysis tensor dependence for the first time in the RDT setting. While presented here in the RANS context, the method is applicable to any tensor function representation problem with analogous constraints and can be implemented around existing ENN libraries such as `e3nn`.

Several promising directions are possible for future work. The learned tensor functions for \mathbf{M} , \mathbf{L} , and \mathbf{J} can be inserted into a numerical solver and used to evaluate the Kassinos and Reynolds RDT model under the ENN closure scheme. Although App. 8.4 provides preliminary evidence that time integration with ENN closures can produce stable trajectories, more work is needed to investigate their performance for the Kassinos and Reynolds model, which involves multiple closure models operating simultaneously. Additional research on the application front could involve the development of closure models in different flow regimes, for example, by extending the return-to-isotropy experiments in App. 8.4 to real data.

Improving the computational efficiency of ENNs is another important direction for future work. As the learned closures discussed here are intended to be used in an iterative solver, optimizing key equivariant operations like the Clebsch-Gordon tensor product will be critical to efficiently integrating neural network models into computational fluid dynamics codes.

7 Acknowledgements

This material is based upon work supported by the U.S. Department of Energy, Office of Science, Office of Advanced Scientific Computing Research, and Department of Energy Computational Science Graduate Fellowship under Award Number DE-SC0025528. This material is also based upon work supported by the National Science Foundation under Award No. CBET-2347423.

References

- [1] S. B. Pope. *Turbulent flows*. Cambridge ; New York: Cambridge University Press, 2000. ISBN: 978-0-521-59125-6 978-0-521-59886-6.
- [2] S. B. Pope. “A more general effective-viscosity hypothesis”. en. In: *Journal of Fluid Mechanics* 72.2 (Nov. 1975), pp. 331–340. ISSN: 1469-7645, 0022-1120. DOI: 10.1017/S0022112075003382.
- [3] John L. Lumley. “Computational Modeling of Turbulent Flows*”. In: *Advances in Applied Mechanics*. Ed. by Chia-Shun Yih. Vol. 18. Elsevier, Jan. 1979, pp. 123–176. DOI: 10.1016/S0065-2156(08)70266-7.
- [4] John L. Lumley. *Stochastic tools in turbulence*. Dover ed. Dover books on engineering. Mineola, N.Y: Dover Publications, 2007. ISBN: 978-0-486-46270-7.
- [5] Philippe Spalart. *An Old-Fashioned Framework for Machine Learning in Turbulence Modeling*. arXiv:2308.00837. Aug. 2023. DOI: 10.48550/arXiv.2308.00837.
- [6] Karthik Duraisamy, Gianluca Iaccarino, and Heng Xiao. “Turbulence Modeling in the Age of Data”. en. In: *Annual Review of Fluid Mechanics* 51. Volume 51, 2019 (Jan. 2019). Publisher: Annual Reviews, pp. 357–377. ISSN: 0066-4189, 1545-4479. DOI: 10.1146/annurev-fluid-010518-040547.
- [7] S. C. Kassinos, W. C. Reynolds, and M. M. Rogers. “One-point turbulence structure tensors”. en. In: *Journal of Fluid Mechanics* 428 (Feb. 2001), pp. 213–248. ISSN: 0022-1120, 1469-7645. DOI: 10.1017/S0022112000002615.
- [8] H. P. Robertson. “The invariant theory of isotropic turbulence”. en. In: *Mathematical Proceedings of the Cambridge Philosophical Society* 36.2 (Apr. 1940), pp. 209–223. ISSN: 1469-8064, 0305-0041. DOI: 10.1017/S0305004100017199.
- [9] Sutanu Sarkar and Charles G. Speziale. *A simple nonlinear model for the return to isotropy in turbulence*. Tech. rep. NAS 1.26:181797. NTRS Author Affiliations: Institute for Computer Applications in Science and Engineering NTRS Document ID: 19890011041 NTRS Research Center: Legacy CDMS (CDMS). Feb. 1989.
- [10] Myung Kyoon Chung and Soong Kee Kim. “A nonlinear return-to-isotropy model with Reynolds number and anisotropy dependency”. In: *Physics of Fluids* 7.6 (June 1995), pp. 1425–1437. ISSN: 1070-6631. DOI: 10.1063/1.868760.
- [11] Julia Ling, Andrew Kurzawski, and Jeremy Templeton. “Reynolds averaged turbulence modelling using deep neural networks with embedded invariance”. en. In: *Journal of Fluid Mechanics* 807 (Nov. 2016), pp. 155–166. ISSN: 0022-1120, 1469-7645. DOI: 10.1017/jfm.2016.615.
- [12] Mikael L. A. Kaandorp and Richard P. Dwight. “Data-driven modelling of the Reynolds stress tensor using random forests with invariance”. In: *Computers & Fluids* 202 (Apr. 2020), p. 104497. ISSN: 0045-7930. DOI: 10.1016/j.compfluid.2020.104497.
- [13] Jiayi Cai et al. “Revisiting Tensor Basis Neural Networks for Reynolds stress modeling: application to plane channel and square duct flows”. In: *Computers & Fluids* 275 (May 2024). arXiv:2403.11746 [physics], p. 106246. ISSN: 00457930. DOI: 10.1016/j.compfluid.2024.106246.
- [14] A. J. M. Spencer and R. S. Rivlin. “The theory of matrix polynomials and its application to the mechanics of isotropic continua”. en. In: *Archive for Rational Mechanics and Analysis* 2.1 (Jan. 1958), pp. 309–336. ISSN: 1432-0673. DOI: 10.1007/BF00277933.

[15] Xin-Lei Zhang et al. “Ensemble Kalman method for learning turbulence models from indirect observation data”. en. In: *Journal of Fluid Mechanics* 949 (Oct. 2022), A26. ISSN: 0022-1120, 1469-7645. DOI: 10.1017/jfm.2022.744.

[16] Kyle R. Lennon, Gareth H. McKinley, and James W. Swan. “Scientific machine learning for modeling and simulating complex fluids”. In: *Proceedings of the National Academy of Sciences* 120.27 (July 2023). Publisher: Proceedings of the National Academy of Sciences, e2304669120. DOI: 10.1073/pnas.2304669120.

[17] Basu Parmar et al. “Generalized Non-Linear Eddy Viscosity Models for Data-Assisted Reynolds Stress Closure”. In: *AIAA Scitech 2020 Forum*. AIAA SciTech Forum. American Institute of Aeronautics and Astronautics, Jan. 2020. DOI: 10.2514/6.2020-0351.

[18] Alp M. Sunol et al. *Learning constitutive models and rheology from partial flow measurements*. arXiv:2510.24673 [physics]. Oct. 2025. DOI: 10.48550/arXiv.2510.24673.

[19] G. F. Smith. “On isotropic functions of symmetric tensors, skew-symmetric tensors and vectors”. In: *International Journal of Engineering Science* 9.10 (Oct. 1971), pp. 899–916. ISSN: 0020-7225. DOI: 10.1016/0020-7225(71)90023-1.

[20] S. Pennisi. “On third order tensor-valued isotropic functions”. In: *International Journal of Engineering Science* 30.5 (May 1992), pp. 679–692. ISSN: 0020-7225. DOI: 10.1016/0020-7225(92)90011-5.

[21] Aviral Prakash, Kenneth E. Jansen, and John A. Evans. “Invariant data-driven subgrid stress modeling in the strain-rate eigenframe for large eddy simulation”. In: *Computer Methods in Applied Mechanics and Engineering* 399 (Sept. 2022), p. 115457. ISSN: 0045-7825. DOI: 10.1016/j.cma.2022.115457.

[22] Alexandre Duval et al. *A Hitchhiker’s Guide to Geometric GNNs for 3D Atomic Systems*. arXiv:2312.07511 [cs]. Mar. 2024. DOI: 10.48550/arXiv.2312.07511.

[23] Kristof T. Schütt et al. *SchNet: A continuous-filter convolutional neural network for modeling quantum interactions*. arXiv:1706.08566 [stat]. Dec. 2017. DOI: 10.48550/arXiv.1706.08566.

[24] Johannes Gasteiger, Janek Groß, and Stephan Günnemann. *Directional Message Passing for Molecular Graphs*. arXiv:2003.03123 [cs]. Apr. 2022. DOI: 10.48550/arXiv.2003.03123.

[25] Nathaniel Thomas et al. *Tensor field networks: Rotation- and translation-equivariant neural networks for 3D point clouds*. en. arXiv:1802.08219 [cs]. May 2018.

[26] Maurice Weiler et al. *3D Steerable CNNs: Learning Rotationally Equivariant Features in Volumetric Data*. en. arXiv:1807.02547 [cs, stat]. Oct. 2018.

[27] Johannes Brandstetter et al. “Geometric and Physical Quantities improve E(3) Equivariant Message Passing”. en. In: Oct. 2021.

[28] Risi Kondor, Zhen Lin, and Shubhendu Trivedi. *Clebsch-Gordan Nets: a Fully Fourier Space Spherical Convolutional Neural Network*. arXiv:1806.09231 [stat] version: 2. Nov. 2018. DOI: 10.48550/arXiv.1806.09231.

[29] John Jumper et al. “Highly accurate protein structure prediction with AlphaFold”. en. In: *Nature* 596.7873 (Aug. 2021). Publisher: Nature Publishing Group, pp. 583–589. ISSN: 1476-4687. DOI: 10.1038/s41586-021-03819-2.

[30] Simon Batzner et al. “E(3)-equivariant graph neural networks for data-efficient and accurate interatomic potentials”. en. In: *Nature Communications* 13.1 (May 2022). Publisher: Nature Publishing Group, p. 2453. ISSN: 2041-1723. DOI: 10.1038/s41467-022-29939-5.

[31] C. Lawrence Zitnick et al. *An Introduction to Electrocatalyst Design using Machine Learning for Renewable Energy Storage*. arXiv:2010.09435 [cond-mat]. Oct. 2020. DOI: 10.48550/arXiv.2010.09435.

[32] J. Dauparas et al. “Robust deep learning-based protein sequence design using Protein-MPNN”. In: *Science* 378.6615 (Oct. 2022). Publisher: American Association for the Advancement of Science, pp. 49–56. DOI: 10.1126/science.add2187.

[33] Xu-Hui Zhou, Jiequn Han, and Heng Xiao. “Frame-independent vector-cloud neural network for nonlocal constitutive modeling on arbitrary grids”. In: *Computer Methods in Applied Mechanics and Engineering* 388 (Jan. 2022), p. 114211. ISSN: 0045-7825. DOI: 10.1016/j.cma.2021.114211.

[34] Jiequn Han, Xu-Hui Zhou, and Heng Xiao. “An equivariant neural operator for developing nonlocal tensorial constitutive models”. In: *Journal of Computational Physics* 488 (Sept. 2023), p. 112243. ISSN: 0021-9991. DOI: 10.1016/j.jcp.2023.112243.

[35] Liyao Gao et al. “RotEqNet: Rotation-equivariant network for fluid systems with symmetric high-order tensors”. In: *Journal of Computational Physics* 461 (July 2022), p. 111205. ISSN: 0021-9991. DOI: 10.1016/j.jcp.2022.111205.

[36] Grzegorz Kaszuba et al. “Implicit modeling of equivariant tensor basis with Euclidean turbulence closure neural network”. In: *Physics of Fluids* 37.2 (Feb. 2025), p. 025137. ISSN: 1070-6631. DOI: 10.1063/5.0249490.

[37] Tobias Pfaff et al. *Learning Mesh-Based Simulation with Graph Networks*. arXiv:2010.03409 [cs]. June 2021.

[38] Artur P. Toshev et al. *Learning Lagrangian Fluid Mechanics with $E(\mathcal{S})$ -Equivariant Graph Neural Networks*. arXiv:2305.15603 [cs]. May 2023. DOI: 10.48550/arXiv.2305.15603.

[39] B. List, M. Lino, and N. Thuerey. “Rotational equivariant graph neural networks via local eigenbasis transformations”. In: *Physics of Fluids* 37.8 (Aug. 2025), p. 087178. ISSN: 1070-6631. DOI: 10.1063/5.0279499.

[40] Mario Lino et al. “Multi-scale rotation-equivariant graph neural networks for unsteady Eulerian fluid dynamics”. en. In: *Physics of Fluids* 34.8 (Aug. 2022), p. 087110. ISSN: 1070-6631, 1089-7666. DOI: 10.1063/5.0097679.

[41] Michele Milano and Petros Koumoutsakos. “Neural Network Modeling for Near Wall Turbulent Flow”. In: *Journal of Computational Physics* 182.1 (Oct. 2002), pp. 1–26. ISSN: 0021-9991. DOI: 10.1006/jcph.2002.7146.

[42] M. Raissi, P. Perdikaris, and G.E. Karniadakis. “Physics-informed neural networks: A deep learning framework for solving forward and inverse problems involving nonlinear partial differential equations”. en. In: *Journal of Computational Physics* 378 (Feb. 2019), pp. 686–707. ISSN: 00219991. DOI: 10.1016/j.jcp.2018.10.045.

[43] George Em Karniadakis et al. “Physics-informed machine learning”. en. In: *Nature Reviews Physics* 3.6 (June 2021). Publisher: Nature Publishing Group, pp. 422–440. ISSN: 2522-5820. DOI: 10.1038/s42254-021-00314-5.

[44] Rui Wang, Robin Walters, and Rose Yu. *Incorporating Symmetry into Deep Dynamics Models for Improved Generalization*. arXiv:2002.03061 [cs]. Mar. 2021. DOI: 10.48550/arXiv.2002.03061.

[45] Shuxiao Chen, Edgar Dobriban, and Jane H Lee. “A Group-Theoretic Framework for Data Augmentation”. en. In: () .

[46] Ning Liu et al. “Harnessing the Power of Neural Operators with Automatically Encoded Conservation Laws”. en. In: *Proceedings of the 41st International Conference on Machine Learning*. ISSN: 2640-3498. PMLR, July 2024, pp. 30965–30997.

[47] Jack Richter-Powell, Yaron Lipman, and Ricky T. Q. Chen. *Neural Conservation Laws: A Divergence-Free Perspective*. arXiv:2210.01741 [cs]. Dec. 2022. DOI: 10.48550/arXiv.2210.01741.

[48] Nithin Chalapathi, Yiheng Du, and Aditi Krishnapriyan. *Scaling physics-informed hard constraints with mixture-of-experts*. arXiv:2402.13412 [cs]. Feb. 2024. DOI: 10.48550/arXiv.2402.13412.

[49] Nicolas Vasilache et al. *Tensor Comprehensions: Framework-Agnostic High-Performance Machine Learning Abstractions*. arXiv:1802.04730 [cs]. June 2018. DOI: 10.48550/arXiv.1802.04730.

[50] Stavros Chistofer Kassinos. “A structure-based model for the rapid distortion of homogeneous turbulence”. English. ISBN: 9798209432388. Ph.D. United States – California: Stanford University, 1995.

[51] Mildred S. Dresselhaus, Gene Dresselhaus, and Ado Jorio, eds. *Group Theory*. eng. Springer-Link Bücher. Berlin, Heidelberg: Springer Berlin Heidelberg, 2008. ISBN: 978-3-540-32897-1 978-3-540-32899-5. DOI: 10.1007/978-3-540-32899-5.

[52] Howard Georgi. *Lie algebras in particle physics: from isospin to unified theories*. eng. Second edition. Frontiers in physics 54. Boca Raton, Fl: CRC Press, 2018. ISBN: 978-0-429-49921-0 978-0-429-96776-4. DOI: 10.1201/9780429499210.

[53] Tess Smidt. *Intuition for the Data Types and Interactions of Euclidean Neural Networks*. Published: Keynote presentation at the 2nd Annual Workshop on Topology, Algebra, and Geometry in Machine Learning (TAG-ML) at ICML 2023. July 2023.

[54] Taco S. Cohen and Max Welling. *Steerable CNNs*. arXiv:1612.08498 [cs]. Dec. 2016. DOI: 10.48550/arXiv.1612.08498.

[55] Mario Geiger and Tess Smidt. *e3nn: Euclidean Neural Networks*. arXiv:2207.09453 [cs]. July 2022. DOI: 10.48550/arXiv.2207.09453.

[56] I. M Sobol’. “On the distribution of points in a cube and the approximate evaluation of integrals”. In: *USSR Computational Mathematics and Mathematical Physics* 7.4 (Jan. 1967), pp. 86–112. ISSN: 0041-5553. DOI: 10.1016/0041-5553(67)90144-9.

[57] Robert S. Womersley. *Efficient Spherical Designs with Good Geometric Properties*. arXiv:1709.01624 [math]. Sept. 2017. DOI: 10.48550/arXiv.1709.01624.

[58] B. E. Launder, G. J. Reece, and W. Rodi. “Progress in the development of a Reynolds-stress turbulence closure”. en. In: *Journal of Fluid Mechanics* 68.3 (Apr. 1975), pp. 537–566. ISSN: 1469-7645, 0022-1120. DOI: 10.1017/S0022112075001814.

[59] B. E. Launder. “Second-moment closure and its use in modelling turbulent industrial flows”. en. In: *International Journal for Numerical Methods in Fluids* 9.8 (1989), pp. 963–985. ISSN: 1097-0363. DOI: 10.1002/fld.1650090806.

[60] Ty Homan, Omkar B. Shende, and Ali Mani. “Reynolds stress decay modeling informed by anisotropically forced homogeneous turbulence”. In: *Physical Review Fluids* 9.9 (Sept. 2024). Publisher: American Physical Society, p. 094608. DOI: 10.1103/PhysRevFluids.9.094608.

[61] J. Rotta. “Statistische Theorie nichthomogener Turbulenz”. de. In: *Zeitschrift für Physik* 129.6 (Nov. 1951), pp. 547–572. ISSN: 0044-3328. DOI: 10.1007/BF01330059.

8 Appendix

Contents

8.1	Definitions for Eqs. 6-8	31
8.2	Architecture and training details	31
8.3	Group theory and representation theory	32
8.4	Return-to-isotropy problem	33
8.4.1	Overview	33
8.4.2	Modeling objective	34
8.4.3	Data generation	34
8.4.4	Tensor representation mechanism	35
8.4.5	Experiments	36
8.4.6	Characterizing anisotropies	37
8.5	Constraints on fully symmetric part of M	38
8.6	Invertibility of E	39

8.1 Definitions for Eqs. 6-8

Definitions of the tensors appearing in Eqs.6-8, some of which are stated in the main text, are provided together here for reference:

Integral equations:

$$\begin{aligned} M_{ijkl} &\equiv \iiint_{-\infty}^{\infty} \Phi_{ij} \frac{\kappa_k \kappa_l}{\kappa^2} d\kappa, \\ D_{ij} &\equiv \iiint_{-\infty}^{\infty} \Phi_{nn} \frac{\kappa_i \kappa_j}{\kappa^2} d\kappa, \\ Q_{ijk} &\equiv \varepsilon_{ipq} \iint_{-\infty}^{\infty} \Phi_{jq} \frac{\kappa_p \kappa_k}{\kappa^2} d^3 \kappa, \\ L_{ijkl} &\equiv \iiint_{-\infty}^{\infty} \Phi_{nn} \frac{\kappa_i \kappa_j \kappa_k \kappa_l}{\kappa^4} d\kappa, \\ J_{ijrpq} &\equiv \varepsilon_{its} \iint_{-\infty}^{\infty} \Phi_{sj} \frac{\kappa_t \kappa_r \kappa_p \kappa_q}{\kappa^4} d\kappa. \end{aligned}$$

Velocity gradient tensors:

$$\begin{aligned} S_{ij} &\equiv \frac{1}{2} \left(\frac{\partial U_i}{\partial x_j} + \frac{\partial U_j}{\partial x_i} \right) = \langle S_{ij} \rangle + s_{ij}, \\ S_{ij}^* &\equiv S_{ij} - \frac{1}{3} \delta_{ij} S_{kk}, \\ \Omega_{ij} &\equiv \frac{1}{2} \left(\frac{\partial U_i}{\partial x_j} - \frac{\partial U_j}{\partial x_i} \right) = \langle \Omega_{ij} \rangle + \omega_{ij}. \end{aligned}$$

Detailed descriptions of the turbulent structure tensors are available in [50].

8.2 Architecture and training details

All models were trained using the parameter values shown in Tab. 3.

Parameter	Value
Epochs	250
Batch size	32
LR schedule	OneCycleLR
Max LR	5×10^{-3}
Precision	float32

Table 3: Parameters used for ENN training.

The backbone of all the equivariant MLPs is the `FullyConnectedTensorProduct` from the `e3nn` library. This module is initialized with

```
irrep_normalization="norm" and path_normalization="path",
```

which insert a per-path multiplicative weight in Eq. 13 based on the dimensions of the irreducible representations involved and the number of paths present (See the the `e3nn` documentation linked in Sec. 5.3).

	$\mathbf{L}(\mathbf{D})$		$\mathbf{L}(\mathbf{D}, \mathbf{Q}^*)$		$\mathbf{M}^*(\langle u_i u_j \rangle, \mathbf{D})$		$\mathbf{M}(\langle u_i u_j \rangle, \mathbf{D}, \mathbf{Q}^*)$	
Constrained	✓	✗	✓	✗	✓	✗	✓	✗
ℓ_{\max}	6	6	6	6	6	6	6	6
Layers	5	5	5	6	4	4	6	6
Hidden dim.	128	256	128	256	256	256	512	256
Parameters	18,623	27,874	21,583	45,249	41,661	42,067	198,341	80,927

Table 4: Parameters for models presented in Sec. 5.

The parameters for the models presented in the main text are shown in Tab. 4. Constrained refers to whether the model was supervised on all the irreducible representation components of the output tensor (unconstrained) or only those not fixed by constraints (constrained). Hidden dimension refers to the total number of irreducible components in a given internal ENN layer. All internal layers share the same hidden dimension. The components in a hidden layer are distributed amongst all the irreducible representations up to and including ℓ_{\max} , including both even and odd parity, such that the total number of components for each ℓ are approximately equal.

8.3 Group theory and representation theory

Definition 8.1 (Group). A group is defined by a set G and a binary operator \cdot that satisfy the following properties:

1. Closure: For all $g, h \in G$, we have $g \cdot h \in G$.
2. Identity: There exists an identity element $e \in G$ such that $e \cdot g = g \cdot e = g$.
3. Inverse: For each $g \in G$, there exists an inverse element $g^{-1} \in G$ such that $g^{-1} \cdot g = g \cdot g^{-1} = e$.
4. Associativity: For each $g, h, i \in G$, it holds that $(g \cdot h) \cdot i = g \cdot (h \cdot i)$.

Definition 8.2 (Group action). A group action of G on a set X is a *function* $\cdot : G \times X \mapsto X$, written $g \cdot x$, satisfying¹⁴

1. Identity: For all $x \in X$, $e \cdot x = x$.
2. Compatibility: For all $g, h \in G$ and $x \in X$, we have $(g \cdot h) \cdot x = g \cdot (h \cdot x)$.

Definition 8.3 (Group representation). A representation of G on a vector space V is a group homomorphism $\rho : G \mapsto GL(V)$, where $GL(V)$ is the group of all invertible linear transformations from V to itself.

Definition 8.4 (Homomorphism). A homomorphism is a function $\rho : G \mapsto H$ such that for all $g_1, g_2 \in G$, we have

$$\rho(g_1 \cdot g_2) = \rho(g_1) \cdot \rho(g_2).$$

Definition 8.5 (G -invariance). Let $\rho : G \mapsto GL(V)$ be a representation of group G on a vector space V . A linear subspace $W \subseteq V$ is called G -invariant if $\rho(g)w \in W$ for all $g \in G$ and all $w \in W$. If W is G -invariant, the co-restriction of ρ to $GL(W)$ is called a subrepresentation.

¹⁴Note that the dots in this define technically have different meanings depending on the objects involved.

Definition 8.6 (irreducible representation). A representation $\rho : G \mapsto GL(V)$ is irreducible if it has only trivial ($W \notin \{V, \{0\}\}$) subrepresentations.

Definition 8.7 (Isotypic component). Let G be a group and V a finite-dimensional representation of G . The isotypic component of V corresponding to an irreducible representation W of G is the direct sum of all G -invariant subspaces of V that are isomorphic to W . Equivalently, it is the largest G -invariant subspace of V that decomposes as a direct sum of copies of W .

8.4 Return-to-isotropy problem

If the mean velocity gradients in a homogeneous, anisotropic turbulent flow are removed, it is observed that the turbulence subsequently relaxes to isotropy. As with RDT, the flow conditions cause several terms in the Reynolds stress transport equation to vanish, isolating a closure modeling problem that can be addressed with ENNs.

8.4.1 Overview

In Eq. 4, homogeneity implies that the fluctuation statistics vanish, so the transport $\partial T_{kij}/\partial x_k$, the convection term, and the harmonic pressure-strain $\mathcal{R}_{ij}^{(h)}$ are zero. Without mean velocity gradients, \mathcal{P}_{ij} and $\mathcal{R}_{ij}^{(r)}$ also vanish, so the Reynolds stress transport equation reduces to

$$\frac{d\langle u_i u_j \rangle}{dt} = \mathcal{R}_{ij}^{(s)} - \varepsilon_{ij}. \quad (22)$$

Hence, decaying homogeneous anisotropic turbulence serves as a setting for developing models of the slow pressure-rate-of-strain tensor $\mathcal{R}_{ij}^{(s)}$ the dissipation tensor ε_{ij} .

Due to the nature of the problem, it is customary to consider the evolution of the (normalized) anisotropy tensor

$$b_{ij} \equiv \frac{\langle u_i u_j \rangle}{\langle u_k u_k \rangle} - \frac{1}{3} \delta_{ij} = \frac{\langle u_i u_j \rangle}{2k} - \frac{1}{3} \delta_{ij}$$

rather than the Reynolds stresses directly. It is also common¹⁵ to adopt the model

$$\varepsilon_{ij} = \frac{2}{3} \varepsilon \delta_{ij} \quad (23)$$

for the dissipation tensor in high-Reynolds number flows [1, 9]. Using Eq. 23, the evolution of the anisotropy is

$$\frac{db_{ij}}{dt} = \frac{\varepsilon}{k} \left(b_{ij} + \frac{\mathcal{R}_{ij}^{(s)}}{2\varepsilon} \right).$$

The exact evolution equation for k is $dk/dt = -\varepsilon$, obtained by contracting Eq. 22, and a model equation for ε is $d\varepsilon/dt = -C_{\varepsilon 2}\varepsilon^2/k$, where $C_{\varepsilon 2}$ is a constant [9]. This leaves $\mathcal{R}_{ij}^{(s)}$ as the only term that must be modeled to form a closed system for \mathbf{b} , k , and ε .

¹⁵The validity of this has been questioned. An alternative route is to model $\mathcal{R}_{ij}^{(s)}$ and the anisotropy of ε_{ij} jointly [60].

8.4.2 Modeling objective

A general closure model for $\mathcal{R}_{ij}^{(s)}$ can be written as

$$\mathcal{R}_{ij}^{(s)} = \hat{f}_{ij}(\langle u_k u_l \rangle, \varepsilon, \nu),$$

or, using dimensional analysis,

$$\frac{\mathcal{R}_{ij}^{(s)}}{\varepsilon} = f_{ij}(\mathbf{b}, \text{Re}), \quad (24)$$

where \mathbf{f} is an unspecified tensor function and $\text{Re} \equiv k^2/(\varepsilon \nu)$ is the local turbulent Reynolds number. Important modeling considerations are analogous to those in Sec. 5.1:

- Models are sought for Eq. 24 to ensure dimensional consistency.
- The left-hand-side is a second-order Cartesian tensor, so the components of \mathbf{f} must satisfy the implied transformation rules.
- Since $\mathcal{R}_{ij}^{(s)}$ is symmetric and deviatoric, \mathbf{f} should be as well.
- Examining Eq. 3, $\mathcal{R}_{ij}^{(s)}$ is trace-free, so \mathbf{f} must obey the linear constraint $f_{ii} = 0$.
- The model is local.

8.4.3 Data generation

A dataset for the return-to-isotropy problem consists of a set of pairs $\{(\mathbf{b}_i, \text{Re}_i)\}_{i=1}^N$ of anisotropy tensors and Reynolds numbers, which are the inputs to the ENN, and a set of targets $\{\mathbf{f}_i\}_{i=1}^N$. The experiments shown here use synthetic data, both to avoid expensive simulations and to provide an example that illustrates the functional representation mechanism of ENNs.

Recall from Sec. 2.1 that the tensor basis method proceeds by seeking the most general form of \mathbf{f} as a linear combination of basis tensors and scalar coefficient functions of tensor invariants. In this framework, one has

$$f_{ij} = \sum_n \hat{g}^{(n)} \mathcal{T}_{ij}^{(n)}, \quad (25)$$

where the $\hat{g}^{(n)}$ are scalar coefficients that can depend on Re and the invariants of \mathbf{b} and the $\mathcal{T}_{ij}^{(n)}$ are all the symmetric, deviatoric tensors that can be formed from \mathbf{b} . Applying the Cayley-Hamilton theorem, only the tensors

$$\mathcal{T}_{ij}^{(n)} = b_{ij}^n - \frac{1}{3} b_{kk}^n \delta_{ij}$$

for $n \in \{1, 2\}$ are necessary in the sum, so Eq. 25 becomes

$$f_{ij}(\mathbf{b}, \text{Re}) = g^{(1)}(\xi, \eta, \text{Re}) b_{ij} + g^{(2)}(\xi, \eta, \text{Re}) \left(b_{ij}^2 - \frac{1}{3} b_{kk}^2 \delta_{ij} \right), \quad (26)$$

where ξ and η are invariants of \mathbf{b} ¹⁶.

A particular model corresponds to a specification of $g^{(1)}$ and $g^{(2)}$. Examples include the Rotta model [61], the Lumley model [3], the Sarkar-Speziale model [9], and the model of Chung and Kim [10]. The behaviors of these different models are often compared with one another and with experiment by plotting the trajectories of the anisotropy invariants on the so-called Lumley triangle,

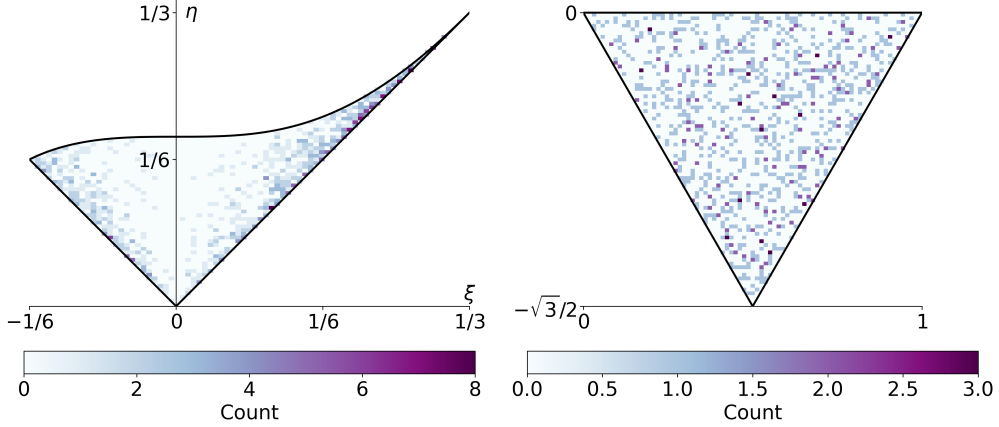


Figure 8: Histogram of samples $\{\mathbf{b}_i\}_{i=1}^N$ used to produce the training data for the ENN. Left: Lumley triangle (or anisotropic invariant map). Right: Barycentric triangle, in which the componentality of \mathbf{b} is given equal spatial representation. The same 1000 samples are shown in both triangles.

or anisotropy-invariant map (AIM). An ENN trained on data from one of these models should recover the corresponding behavior when used to solve for a trajectory.

The synthetic data used here is generated from the Sarkar-Speziale model because it features nonlinear dependence on the anisotropy tensor ($g^{(2)} \neq 0$). Input data are generated by uniformly sampling $\{\mathbf{b}_i\}_{i=1}^N$ from the barycentric triangle of realizable states, as shown in Fig. 8 (The Sarkar-Speziale model does not depend on Reynolds number, so the input data only include anisotropy tensors). Eq. 26 is then used to compute the corresponding targets $\{\mathbf{f}_i\}_{i=1}^N$. In this case, $g^{(1)} = -3.4$ and $g^{(2)} = 4.2$. To demonstrate the advantage of equivariance, each anisotropy tensor is rotated with a different random rotation matrix before being used in Eq. 26. This imitates a situation in which data is collected from sources that use different coordinate systems. With ENNs, these randomly rotated data can be freely mixed in the training set without standardization.

After the ENN is trained, it may be inserted in the system of equations

$$\begin{cases} \dot{b}_{ij} = \frac{\varepsilon}{k} \left(b_{ij} + \frac{1}{2} f_{ij} \right), \\ \dot{k} = -\varepsilon, \\ \dot{\varepsilon} = -C_{\varepsilon 2} \frac{\varepsilon^2}{k}, \end{cases} \quad (27)$$

to form a closed system that can be integrated forward in time. The same can be done for any of the other models, and the behavior produced by each can be compared on the AIM.

8.4.4 Tensor representation mechanism

As the analytical form of the targets is known (Eq. 26), representation theory can be used to understand exactly how the ENN architecture builds the closure model.

Eq. 26 is reproduced here for reference:

$$f_{ij}(\mathbf{b}, \text{Re}) = g^{(1)}(\xi, \eta, \text{Re}) b_{ij} + g^{(2)}(\xi, \eta, \text{Re}) \left(b_{ij}^2 - \frac{1}{3} b_{kk}^2 \delta_{ij} \right).$$

¹⁶An overview of different ways of writing the anisotropy invariants is given in App. 8.4.6.

The first basis tensor in the linear combination, \mathbf{b} , is a symmetric, trace-free tensor. In the spherical basis, it is fully described by a single $\ell = 2$ spherical tensor. The same is true of

$$\mathcal{T}^{(2)} = b_{ij}^2 - \frac{1}{3}b_{kk}^2\delta_{ij}$$

(as it must be for the sum to be valid), only this time the dependence on \mathbf{b} is nonlinear.

The Kronecker product, and by extension the Clebsch-Gordon tensor product, is the most general multilinear interaction of a tensor with itself. In particular, $\mathbf{b} \otimes_{\text{kr}} \mathbf{b}$ contains the information from all of \mathbf{b}^2 , $\mathbf{b}\mathbf{b}^T$, $\text{tr}(\mathbf{b})\mathbf{b}$, and so on through its various contractions. This means that one ENN layer is sufficient to construct $\mathcal{T}^{(2)}$ in the spherical basis. In fact, since $g^{(1)}$ and $g^{(2)}$ are constants in the Sarkar-Speziale model, Eq. 26 can be learned exactly by a one-layer, two-parameter ENN using the following design.

The architecture of Sec. 4.5 operates by decomposing Cartesian tensor inputs and iteratively interacting concatenated spherical tensors. If the input is a second-order symmetric, trace-free tensor, as it is for the Sarkar-Speziale model, it will be decomposed into an $\ell = 2$ spherical tensor $\mathbf{b}^{(2,e)}$ (See Def. 10 for notation). The first interaction in the network will then be

$$(\ell = 2) \otimes (\ell = 2) \rightarrow (\ell = 0) \oplus (\ell = 1) \oplus (\ell = 2) \oplus (\ell = 3) \oplus (\ell = 4),$$

where the notation here is applied loosely to indicate selection rules. However, this tensor product, which has the spherical tensor equivalent of $\mathcal{T}^{(2)}$ as the $\ell = 2$ component, does not give the network a path to construct the linear \mathbf{b} term. This can be easily fixed by concatenating a nonzero scalar to one of the $\mathbf{b}^{(2,e)}$ spherical tensor inputs. In this case, the tensor product becomes

$$(\ell = 2) \otimes [(\ell = 0) \oplus (\ell = 2)] \rightarrow (\ell = 0) \oplus (\ell = 1) \oplus 2(\ell = 2) \oplus (\ell = 3) \oplus (\ell = 4),$$

where there are now two $\ell = 2$ outputs, corresponding to the spherical tensor equivalents of $\mathcal{T}^{(1)}$ and $\mathcal{T}^{(2)}$.

Since the objective is to output a second-order tensor \mathbf{f} that is also symmetric and trace-free, only the $\ell = 2$ outputs of the tensor product will be retained by the network. The tensor product will therefore have two weights, corresponding to the paths

$$(\ell = 0) \otimes (\ell = 2) \rightarrow (\ell = 2) \quad \text{and} \quad (\ell = 2) \otimes (\ell = 2) \rightarrow (\ell = 2).$$

The spherical to Cartesian decoding maps these tensors to the first and second terms of Eq. 26, respectively. The learned Clebsch-Gordon weights correspond to $g^{(1)}$ and $g^{(2)}$. No nonlinear gate is necessary here, so an ENN with these two weights is sufficient to solve the learning problem perfectly.

Note that the construction of $\mathcal{T}^{(1)}$ and $\mathcal{T}^{(2)}$ in the spherical basis is handled automatically by the ENN and does not have to be learned. All the ENN needs access to is the *data*, while the tensor basis method requires access to the data *and* the tensor basis.

8.4.5 Experiments

Fig. 9 shows the training curve for the two-parameter ENN. The loss reaches machine precision, in agreement with the above analysis. Fig. 10 shows the AIM trajectories obtained by integrating Eq. 27 using the ENN and Sarkar-Speziale models for \mathbf{f} . Initial conditions are sampled evenly along the top of the anisotropy triangle in principal axes coordinates, and a random global coordinate system rotation is applied before starting the integration. Markers are shown for both models at each step of the time integration. All trajectories are directed toward the origin, which represents the pure isotropy state. As expected, the two models produce identical behavior at every step of the integration.

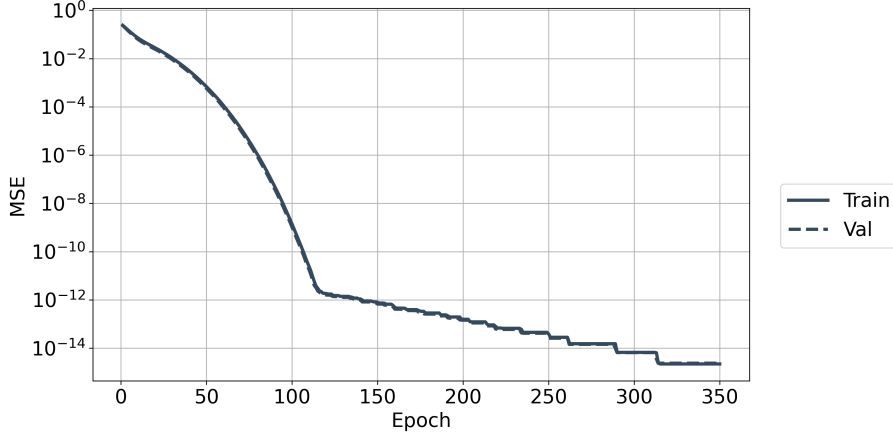


Figure 9: Loss curves for a two-parameter ENN trained on synthetic data from the Sarkar-Speziale return-to-isotropy model. The learning problem is able to be solved perfectly, as expected.

8.4.6 Characterizing anisotropies

In general, a second-order Cartesian tensor \mathbf{b} has three independent invariants, usually taken as

$$\begin{aligned} \text{I} &= b_{ii}, \\ \text{II} &= \frac{1}{2}[(b_{ii})^2 - b_{ii}^2], \\ \text{III} &= \frac{1}{6}(b_{ii})^3 - \frac{1}{2}b_{ii}b_{jj}^2 + \frac{1}{3}b_{ii}^3. \end{aligned}$$

If \mathbf{b} is traceless, it only has two independent invariants, namely

$$\text{II} = -\frac{1}{2}b_{ii}^2 \quad \text{and} \quad \text{III} = \frac{1}{3}b_{ii}^3.$$

It is common in the return-to-isotropy problem to consider the invariants

$$6\eta^2 = -2\text{II} \quad \text{and} \quad 6\xi^3 = 3\text{III}$$

and examine parametric trajectories in the ξ - η plane. The Reynolds stress tensor at a particular time t corresponds to a point (ξ, η) , so the evolution of \mathbf{b} traces a trajectory in the plane over time. All such trajectories must remain entirely within the so-called Lumley triangle, which defines the region in the plane corresponding to physically realizable Reynolds stress tensors¹⁷.

The invariants η and ξ are related to the eigenvalues¹⁸ of \mathbf{b} by

$$\eta^2 = \frac{1}{3}(\lambda_1^2 + \lambda_1\lambda_2 + \lambda_2^2) \quad \text{and} \quad \xi^3 = -\frac{1}{2}\lambda_1\lambda_2(\lambda_1 + \lambda_2),$$

and these eigenvalues are related to the eigenvalues $\langle \tilde{u}_1^2 \rangle$, $\langle \tilde{u}_2^2 \rangle$, and $\langle \tilde{u}_3^2 \rangle$ of the Reynolds stress tensor by

$$\lambda_1 = \frac{\langle \tilde{u}_2^2 \rangle}{\langle \tilde{u}_1^2 \rangle + \langle \tilde{u}_2^2 \rangle + \langle \tilde{u}_3^2 \rangle} - \frac{1}{3} \quad \text{and} \quad \lambda_2 = \frac{\langle \tilde{u}_2^2 \rangle}{\langle \tilde{u}_1^2 \rangle + \langle \tilde{u}_2^2 \rangle + \langle \tilde{u}_3^2 \rangle} - \frac{1}{3}.$$

¹⁷The notion of realizability applies to all Reynolds stress tensors, not just those in the return-to-isotropy context. In general, a point (ξ, η) corresponds to the Reynolds stress tensor at a particular time and spatial location.

¹⁸The eigenvalues of tensors like \mathbf{b} and $\langle u_i u_j \rangle$ are equivalent to the component values in the principal axes coordinate system.

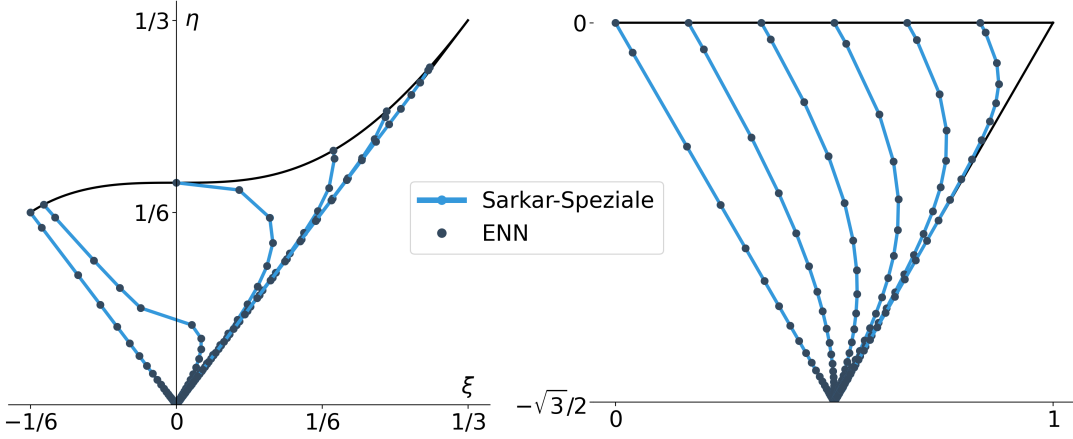


Figure 10: Invariant space trajectories of the anisotropy tensor \mathbf{b} plotted on the Lumley triangle (left) and barycentric invariant map (right). The trajectories are obtained by integrating Eq. 27 from six initial conditions evenly spaced along the top of the barycentric triangle. Markers are plotted at each integration step. All trajectories proceed toward the origin as time advances.

Isotropic turbulence has $\langle \tilde{u}_1^2 \rangle = \langle \tilde{u}_2^2 \rangle = \langle \tilde{u}_3^2 \rangle$, which corresponds to $(\xi, \eta) = (0, 0)$. Hence, in the return-to-isotropy problem, the ξ - η trajectories start at some point within the triangle dictated by the initial condition and end at the origin. The particular path taken depends on the specification of Φ_{ij} , and one can use these trajectories to compare the behavior implied by different models and that measured in experiments.

8.5 Constraints on \mathbf{M}^*

From Tab. 2, \mathbf{M} satisfies

$$M_{ikkk} = 0, \quad M_{ijkk} = \langle u_i u_j \rangle, \quad M_{kkij} = D_{ij}, \quad \text{and} \quad \text{Sym}(\varepsilon_{ipq} M_{jqp}) = Q_{ijk}^*. \quad (28)$$

The first three of these constraints are obtained by contracting two indices of \mathbf{M} . For \mathbf{M}^* , which is fully symmetric, any contraction of two indices produces the same second-order tensor, and the three constraints for \mathbf{M} collapse into one:

$$M_{ijkk}^* = \frac{1}{12} \sum_{\sigma \in S_4 / S_2} M_{\sigma(i,j,k,k)} = \frac{1}{6} (\langle u_i u_j \rangle + D_{ij}), \quad (29)$$

where S_4 and S_2 are the symmetric groups on four and two elements, respectively. All of the terms in the sum are zero except for $M_{ijkk} = M_{jikk} = \langle u_i u_j \rangle$ and $M_{kkij} = M_{kkji} = D_{ij}$ due to the symmetry of \mathbf{M} . Since M_{ijkk}^* is a symmetric second-order tensor, Eq. 29 decomposes into 0e + 2e and represents six constraints.

As \mathbf{M}^* decomposes into 0e + 2e + 4e, for there to remain an undetermined part of the tensor, it must be that the final constraint in Eq. 28 does not impose any additional restrictions on \mathbf{M}^* . Indeed, writing $\mathbf{M} = \mathbf{M}^* + \mathbf{M}'$, where \mathbf{M}' is the non-fully symmetric part of \mathbf{M} , the final constraint becomes

$$\text{Sym}[\varepsilon_{ipq} (M'_{jqp} + M_{jqp}^*)] = \text{Sym}(\varepsilon_{ipq} M'_{jqp}) + \text{Sym}(\varepsilon_{ipq} M_{jqp}^*) = Q_{ijk}^*,$$

but for $\text{Sym}(\varepsilon_{ipq} M_{jqp}^*)$, contracting a pair of symmetric and antisymmetric indices makes the term zero. Hence, the \mathbf{Q}^* relation only constrains the non-fully symmetric part of \mathbf{M} , leaving the $\ell = 4$ components of \mathbf{M}^* to be modeled.

8.6 Invertibility of \mathbf{E}

As explained in Sec. 4.4.2, the map from the spherical basis to the Cartesian basis is $\mathbf{P}_s^T \mathbf{S}_\pi^{-1}(\mathbf{E}^T)^{-1}$, which involves the inverse of the \mathbf{E} matrix from Alg. 1. The columns of the \mathbf{E} matrix are populated by solutions to the least squares problem in Line 11 of the algorithm. In general, even if all the right-hand-side vectors of a set of least squares problems are linearly independent, the least squares solutions may not be. However, in the algorithm, all of the solutions that populate \mathbf{E} exactly satisfy the least squares problem.

Let the set of these solutions vectors be $\{\mathbf{x}_1, \mathbf{x}_2, \dots, \mathbf{x}_k\}$. Writing

$$c_1 \mathbf{x}_1 + c_2 \mathbf{x}_2 + \dots + c_k \mathbf{x}_k = \mathbf{0}$$

and multiplying by \mathbf{A}^T from Alg. 1,

$$A(c_1 \mathbf{x}_1 + c_2 \mathbf{x}_2 + \dots + c_k \mathbf{x}_k) = c_1 \mathbf{b}_1 + c_2 \mathbf{b}_2 + \dots + c_k \mathbf{b}_k = \mathbf{0}.$$

The columns of \mathbf{B} are linearly independent, so the only way for this equation to be true is if $c_1 = c_2 = \dots = c_k = 0$. Hence, the vectors that populate the square matrix \mathbf{E} are linearly independent, and the inverse exists.